



Supplementary Materials for

Scalable thermochromic smart windows with passive radiative cooling regulation

Shancheng Wang *et al.*

Corresponding authors: Ronggui Yang, ronggui@hust.edu.cn; Gang Tan, gtan@uwyo.edu; Yi Long, longyi@ntu.edu.sg

Science **374**, 1501 (2021)
DOI: 10.1126/science.abg0291

The PDF file includes:

Materials and Methods
Figs. S1 to S27
Tables S1 to S6
References

Materials and Methods

Fabrication of VO₂-PMMA multilayer structure

VO₂ NPs (Pure and 2 wt.% W-doped, Hangzhou Jikang New Material CO.,LTD), PMMA (Mw: ~120,000, Sigma-Aldrich), acetone (95%, Aik Moh), double side ITO coated glass (Wintek Technology) were used in this work without further purification. The ITO glass was cleaned by ethanol and dried before spin coating.

The PMMA was dissolved into acetone to spin coat the PMMA layer in multilayer structure. 0.5 g and 1 g PMMA were dissolved into 10 ml acetone respectively to form the PMMA solution with different concentration. In order to prepare PMMA thin film with different thickness, the PMMA solutions were coated on the ITO coated glass with different spinning speeds of up to 3000 rpm with the use of a spin coater (POLOS 150i, Specialty Coating Systems Inc.).

For the deposition of VO₂ layer, VO₂ NPs and PMMA particles with different weight ratio (Table S6) was dispersed in 5 ml acetone to prepare the VO₂-PMMA suspension. The suspension was firstly stirred at 500 rpm for 30 min to dissolve the PMMA. Subsequently, the suspension was sonicated in the ultrasonic bath for 1 hour to form the VO₂ NPs-PMMA mixture for spin coating. The VO₂ thin film was spin coated with the same spin coater used to prepared PMMA thin film. The spinning speed were set as 3000 rpm. The sample for the large-scale fabrication demonstration had the size of 5*5 cm while the sample for optical properties measurement had the size of 2.5*2.5 cm.

Characterization of material

The morphology of VO₂ NPs was investigated scanning electron microscope (SEM, Carl Zeiss Supra 55). The crystal structure of VO₂ NPs was determined through x-ray diffraction (XRD, PANalytical Empyrean). Moreover, the bonding information of PMMA and VO₂ NPs were investigated thought FTIR (Perkin Elmer Frontier). The thickness of films was measured by a surface profiler (NanoMap, AEP Technology).

Optical and thermal properties characterization of VO₂-PMMA multilayer structure

The UV-Vis-NIR spectra for the samples were measured with the UV-Vis-NIR spectrometer (Avantes AvaSpec-ULS2048L StarLine Versatile Fiber-optic Spectrometer and AvaSpec-NIR256-2.5-HSC-EVO). To control the sample temperature, a heating/cooling stage (Linkam PE120) was installed. Spot size for UV-Vis spectrometer was 0.5*0.5 cm.

The T_{lum} and T_{sol} were calculated with the formula:

$$T_{lum/sol} = \frac{\int \varphi_{lum/sol} T(\lambda) d\lambda}{\int \varphi_{lum/sol} d\lambda}$$

The $T(\lambda)$ is the spectral transmittance (360 nm-780 nm for T_{lum} and 360 nm-2500 nm for T_{sol}).

$\varphi_{lum}(\lambda)$ is the standard luminous efficiency function of photopic vision for the wavelength of 380–780 nm.(34) $\varphi_{sol}(\lambda)$ is the solar irradiance spectra for air mass 1.5 (corresponding to the sun standing 37 ° above the horizon with 1.5 atmosphere thickness, corresponds to a solar zenith angle of 48.2°).(35) The ΔT_{sol} was calculated with the formula:

$$\Delta T_{sol} = T_{sol,20^{\circ}\text{C}} - T_{sol,90^{\circ}\text{C}}$$

The hysteresis loop of VO₂ was measured with the UV-Vis-NIR spectrometer with the heating/cooling stage installed. The transmittance of 1750 nm was recorded for plotting. The sample was firstly heated from 20 °C to 100 °C, and 100 °C back to 20 °C for a cooling process. The data interval for the hysteresis loop measurement was 5 °C. For each data point, the

transmittance of the sample was recorded after the temperature of the sample was stabilized. The τ_c was determined by calculating the derivation of transmittance against temperature. The integrated ε_{LWIR} of the samples were measured by a dual-band emissivity measuring instrument (IR-2, Shanghai Chengbo Photoelectric Technology) with heating stage equipped. ε_{LWIR} value of 5 spots were recorded for every sample and the average value was used as the final ε_{LWIR} . The $\Delta\varepsilon_{LWIR}$ were calculated with the formula:

$$\Delta\varepsilon_{LWIR} = \varepsilon_{LWIR-H} - \varepsilon_{LWIR-L}$$

Where the ε_{LWIR-H} was the integrated LWIR emissivity of sample that measured at high temperature while the ε_{LWIR-L} was the integrated LWIR emissivity of sample that measured at low temperature.

Meanwhile, ε_{LWIR} spectral curve was plotted according to the Kirchhoff's law of thermal radiation: $\varepsilon(\lambda) = A(\lambda) = 1 - T(\lambda) - R(\lambda)$. (36, 37) Where $R(\lambda)$ is the spectral LWIR reflectance and $T(\lambda)$ is the spectral LWIR transmittance that measured by FTIR spectrometer (Perkin Elmer Frontier) with an integration sphere attached. Spot size for FTIR spectrometer was 2*2 cm. The sample temperature was controlled by a self-designed heating plate. The IR images of the multilayer structure and VO₂ on glass were taken by an IR camera (FLIR E4) with a copper background ($\varepsilon_{LWIR}=0.5$). The sample temperature was controlled by the same heating/cooling stage used in UV-Vis spectroscopy, while the color in IR image only represent the ε_{LWIR} difference between sample and background.

The relationship of $\Delta\varepsilon_{LWIR}$ and spacer thickness was simulated based on FDTD method. The structure of the simulated multilayer structure consists of an intrinsic VO₂ thin layer with the thickness of 25 nm, PMMA spacer with the thickness from 1 μ m to 5 μ m, and double-sided ITO glass with the ITO thickness of 100 nm. The surface roughness and defects of the structure were ignored in the simulation. The optical constants of VO₂, PMMA, ITO, and SiO₂ were obtained from reference (38-42), respectively.

Energy saving performance simulation

When investigating the sensitivity of the T_{sol} and ε_{LWIR} impacts on the building cooling and heating energy consumption, a single-story small office building has been proposed (Fig. S11). The heating and cooling energies are modeled from whole building energy simulation using EnergyPlus by applying "ideal-loads-air-systems" served with district cooling and heating sources, the results of which closely represent direct effects of the various T_{sol} and ε_{LWIR} characteristics to space cooling and heating loads. In particular, the building has a dimension of 20m (L) \times 10m (W) \times 4m (H) and the building façade and HVAC specifications of the model are displayed in Table S2A, while the insulation meets the requirements of ASHRAE standard 90.1 (43). In the model, the glazing system has a gross window glass area of 72 m², with a window to wall ratio of 30%, which is evenly distributed to four walls. Typical locations under seven climate zones for worldwide have been chosen for simulation (43): Honolulu, HI, U.S. (Zone 1), Cairo, Egypt (Zone 2), Shanghai, China (Zone 3), Albuquerque, NM, U.S. (Zone 4), Mannheim, Germany (Zone 5), Stockholm, Sweden (Zone 6), and Whitehorse, YT, Canada (Zone 7). In this mapping with single glaze window, T_{sol} and $\varepsilon_{LWIR-Front}$ of the glass were tuned while $\varepsilon_{LWIR-Back}$ was fixed at 0.1. The heating and cooling energy savings were evaluated by applying the site-to-source energy conversion factors of 1.28 and 1.05 for district heating and cooling, respectively. (44)

The building energy savings of the specimens are estimated from whole building energy simulation using a typical 12-story large office building with a floor dimension of 73m (240ft.,

L) \times 49m (160ft., W) \times 4m (13ft., H) as the prototype building that was developed by Pacific Northwest National Laboratory (PNNL) of the U.S. Department of Energy (DOE) (Fig. S19).⁽⁴⁵⁾ Derived from “DOE’s Commercial Reference Building Models”, this actual size prototype building model represented the commercial buildings in the U.S. and was accepted by building energy area as benchmark models. ⁽⁴⁶⁾ This model follows applicable building codes and standards for energy efficiency requirements⁽⁴³⁾, adopted typical operation and occupancy schedule, and defined typical lighting/miscellaneous loads and HVAC systems. The building façade and HVAC specifications of the prototype are displayed in Table S2B. The building glazing system has a total window glass area of 4,636 m² (window to wall ratio: 40%). The EnergyPlus built-in thermochromic function was applied to model the thermochromic feature of the glass specimens in the simulation. The building energy saving performances are obtained by measuring the differences in values between various types of the specimens including commercial low-E glass, thermochromic glass without RC regulation, and clear glass specimen (baseline). The detailed optical properties of the glass specimens measured at 10 °C interval is updated in the prototype building model and summarized in Fig. S21. The glass surface temperature for the prototype building was modeled using EnergyPlus in which the glazing optical and thermal calculations are based on procedures from the WINDOW program developed by the U.S. Lawrence Berkeley Lab (LBL). ⁽⁴⁷⁾ The typical locations under climate zones around the world were chosen for simulation ⁽⁴³⁾: Honolulu, HI, U.S. (Zone 1), Cairo, Egypt (Zone 2), Shanghai, China (Zone 3), Albuquerque, NM, U.S. (Zone 4), Mannheim, Germany (Zone 5), Stockholm, Sweden (Zone 6), and Whitehorse, YT, Canada (Zone 7). The US prototype building model has been applied when the simulation is conducted at the selected cities under the corresponding climate zone. The site-to-source conversion factor varies with the countries and regions that have diverse energy sources and technologies.^(48, 49) Thereby comprehensively considering these factors for electricity and natural gas in 17 countries to represent the energy utilizing situations worldwide,^(44, 49-56) this work adopted 2.40 and 1.04 for electricity and natural gas, respectively. The results are shown in Fig. S23. Besides, additional cities around the world across different zones were adopted for predicting the heating and cooling energy savings (Fig. 3D): Abu Dhabi, U.A.E.; Bangkok, Thailand; Singapore, Singapore; Karachi, Pakistan; Rio de Janeiro, Brazil; New Delhi, India; Hong Kong, China; Lima, Peru; Adelaide, Australia; Atlanta, GA, U.S.; Auckland, New Zealand; ,Nairobi, Kenya; Cape Town, South Africa; Beijing, China; Lyon, France; Denver, CO, U.S.; Salt Lake City, UT, U.S.; Ottawa, ON, Canada; Calgary, AB, Canada; Ekaterinburg, Russia; Helsinki, Finland; International Falls, MN, U.S.; Tampere, Finland; Resolute, NU, Canada. The building energy savings per unit area is based on window glass area.

Supplementary Text

Characterizations of VO₂ NPs, PMMA, and ITO

Fig. S1 shows the UV-Vis-NIR spectrum (Fig. S1A) and FTIR spectrum (Fig. S1B) of PMMA thin film. The standard error of T_{lum} and T_{sol} value for all samples is less than 10%. The PMMA thin film has a T_{lum} of 89.4%, and a T_{sol} of 84.3%. The visible transmittance of ITO coated glass is shown in Fig. S2. ITO coated glass has a T_{lum} of 81.8%. Meanwhile, ITO coated glass has an ϵ_{LWIR} of 0.1 (Fig. S3).

The SEM image of VO₂ NPs is shown in Fig. S4, while its XRD pattern in Fig. S5 indicates the character XRD peak of VO₂ from the lattice planes (011), (-211), (-212), (-222), and (-213). Fig.

S6 is the FTIR transmittance spectrum for VO₂ NPs, the absorption peak at 422, 530, and 715 cm⁻¹ are due to the V–O–V octahedral bending modes and coupled vibration of V=O bond that belongs to VO₂ NPs.

Fig. S7 is the NIR spectrum of ITO coated glass. It can be observed that ITO coated glass has a low transmittance for light with wavelength longer than 1500 nm. T_{NIR} of ITO coated glass is 58.4%.

Fig. S8 is the derivate of transmittance for pure VO₂. The largest derivation during heating appeared at 65 °C while the largest derivation during cooling appeared at 55 °C. As the result, the pure VO₂ NPs' τ_c was determined as 62.5 °C by averaging the two values.

ϵ_{LWIR} switching performance regulation

Fig. S9 shows the relationship between PMMA thickness, VO₂ weight ratio and ϵ_{LWIR} . It can be observed that with fixed VO₂ weight ratio, $\epsilon_{\text{LWIR-L}}$ increases with the increasing of spacer thickness. On the other hand, the change of $\epsilon_{\text{LWIR-H}}$ differs from $\epsilon_{\text{LWIR-L}}$. The change of $\epsilon_{\text{LWIR-H}}$ is affected by both VO₂ weight ratio and PMMA spacer thickness.

Meanwhile, Fig. S10 shows the comparison between experiment data and simulation data of $\Delta\epsilon_{8-13\mu\text{m}}$ and PMMA spacer thickness with fixed VO₂ weight ratio of 20:1. The difference of experiment and simulation might be due to several reasons. In simulation, the defects of film were ignored to simplify the simulation. Meanwhile, in experiment VO₂-PMMA composite layer was used while in simulation, pure VO₂ layer was used. The same trending indicates that there is an optimized spacer thickness for the best emissivity switching performance.

Mapping of energy consumption vs T_{sol} and ϵ_{LWIR}

The mapping of heating and cooling energy consumption vs T_{sol} (10-90%) and ϵ_{LWIR} (0.1-0.9) across seven climate zones are shown in Fig. 3B and Fig. S12-S17. In this simulation, a single-story small office building was used as prototype (Fig. S11). It is worth noting that in Zone 1, the heating energy consumption is negligible. Therefore, Fig. S12 only shows the cooling energy mapping.

Fig. S18 shows the energy consumption of optimized static ϵ window and optimized dynamic ϵ window. The energy consumption of static optimized ϵ window is derived from the point of minimum total energy consumption in 7 climate zones by fixing ϵ . The optimized dynamic ϵ window has a ϵ_{LWIR} of 0.9 for cooling, 0.1 for heating. Their T_{sol} were all fixed at 30% for studying ϵ_{LWIR} effect according to the recommendation of ASHARE standard. It can be observed that the optimized dynamic ϵ window has lower energy consumption than optimized static ϵ window.

Characterizations of W-doped VO₂ NPs

Fig. S20 is the derivate of transmittance for W-doped VO₂. The largest derivation during heating appeared at 30 °C while the largest derivation during cooling appeared at 25 °C. As the result, the W-doped VO₂ NPs' τ_c was determined as 27.5 °C by averaging the two values.

Fig. S21 shows T_{lum} , T_{sol} and ϵ_{LWIR} of W-doped VO₂ RCRT window at different temperature with an interval of 10 °C. The data was used in the building energy simulation.

Additional energy consumption modelling for RCRT windows

The surface temperature of simulated eastern side window and ambient temperature was showed in Fig. S22. It can be observed that the window has a higher surface temperature than the ambient from 8:00 to 18:00 in Singapore.

Fig. S23 shows the energy savings of commercial low-E glass, W-doped Max $\Delta\epsilon$ sample (namely “current work”) and W-doped VO₂ sample without RC modulation in climate zone 1 to 7 against normal glass. Their optical data used in simulation is listed in Table S5. The $\epsilon_{\text{LWIR-Back}}$ of the three glasses are fixed at 0.1 for comparison. It can be observed that, by combining the thermochromic window to low-E glass, the thermochromic window without RC has a better energy saving performance compared with commercial low-E glass. This observation indicates that ΔT_{sol} is effective for energy saving. Moreover, by adding the RC regulation, the RCRT window could further enhance the energy saving from zone 3 to 7. Therefore, in four-season regions, RC regulation is important as it works with solar modulation to improve energy efficiency. Moreover, with a commercial low-E glass as benchmark, tropical climate Honolulu gives the energy savings of 324.1 MJ m⁻². On the other hand, in cold climate cities such as Stockholm and Whitehorse, RCRT window also shows reduced energy consumption (96.8 MJ m⁻² and 324.6 MJ m⁻², respectively) compared with low-E window. The RCRT window shows an average global energy saving of 206.0 MJ m⁻². It is worth noting that with application of RCRT window, the lighting energy will increase slightly compared to that of the commercial low-E glass, in a range of 0.7 – 2.2%. However, the additional energy savings achieved in HVAC’s delivery system are much more than the increased lighting energy consumption.

Relationship of film thickness and spinning speed for PMMA spacer and VO₂-PMMA layer

The relationship of spinning speed and PMMA layer thickness was showed in Fig. S24. It can be observed that with the spinning speed increasing from 2000 to 4000 rpm, the spacer layer thickness decreases.

The relationship of spinning speed and VO₂-PMMA layer was showed in Fig. S25. As the VO₂ film coated with 3000 rpm has the most stable film thickness across the different weight ratio, the spinning speed of 3000 rpm was chosen to fabricate the multilayer structure. For VO₂ sample without RC regulation, the sample was prepared through spin coating VO₂ NPs-PMMA suspension onto glass substrate with the spin speed of 3000 rpm.

Additional energy consumption simulation for double-glazed window

The energy saving for double glazed unit, double glazed low-E window, and double glazed RCRT window in Shanghai with the single panel normal glass as baseline is shown in Fig. S26. For double glazed RCRT window, RCRT layer is on the surface 1 while the low-E layer is on the surface 2. Optical properties of commercial low-E glass and W-doped Max $\Delta\epsilon$ sample listed in Table S5 were used in this simulation. Compared with double glazed unit (307.7 MJ m⁻²) and double glazed low-E window (386.5 MJ m⁻²), double glazed RCRT window shows the best energy saving performance of 540.7 MJ m⁻².

Improving the emissivity difference between smaller temperature differences

To further improve the emissivity modulation ability between smaller temperature differences, the FDTD simulations with the same multi-layered structure used in Fig. S10 were conducted. In this simulation, Molybdenum (Mo) and Niobium (Nb) doped VO₂ based RCRT windows were employed, and pure VO₂ based RCRT window was used as a benchmark. The optical constant of pure and doped VO₂ at different temperatures was referred from reference. (57-59) It can be

observed that for pure VO₂, the LWIR emissivity drastically increases from 0.1 to 0.62 from 20-70 °C, giving $\Delta\epsilon_{\text{LWIR}} (20-70^\circ\text{C}) = 0.52$. In contrast, Nb-doped VO₂ shows an $\Delta\epsilon_{\text{LWIR}} (20-40^\circ\text{C}) = 0.47$ (20 °C: 0.23, 40 °C: 0.70); while Mo-doped VO₂ achieves $\Delta\epsilon_{\text{LWIR}} (30-35^\circ\text{C}) = 0.44$ (30 °C: 0.24, 35 °C: 0.68) as shown in Fig. S27. Therefore, a similar emissivity difference compared with pure VO₂ can be achieved with a relatively small temperature difference through doping.

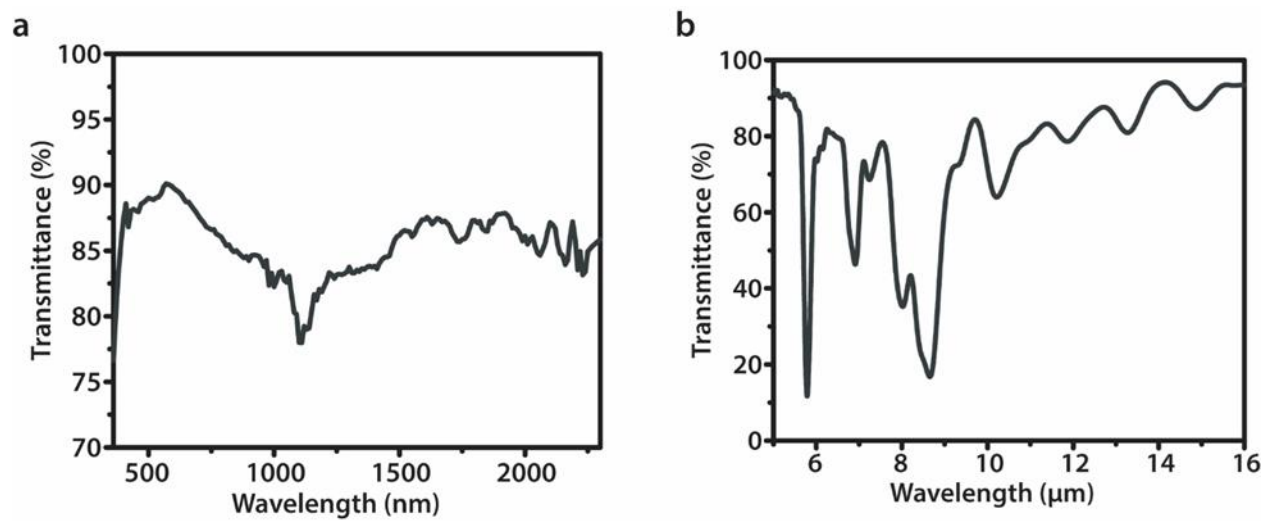


Fig. S1.

(A) UV-Vis-NIR spectrum of PMMA thin film. (B) FTIR spectrum of PMMA thin film.

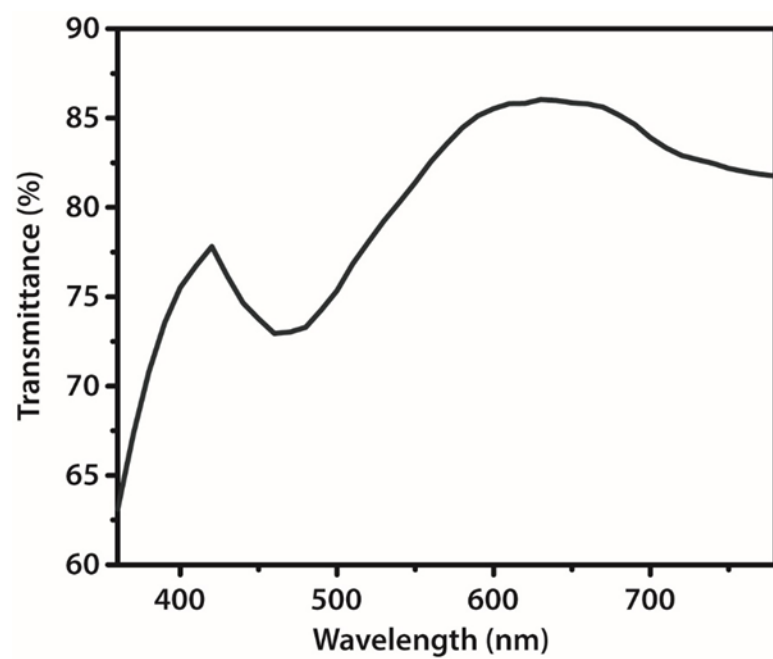


Fig. S2.
Visible transmittance spectra of ITO.

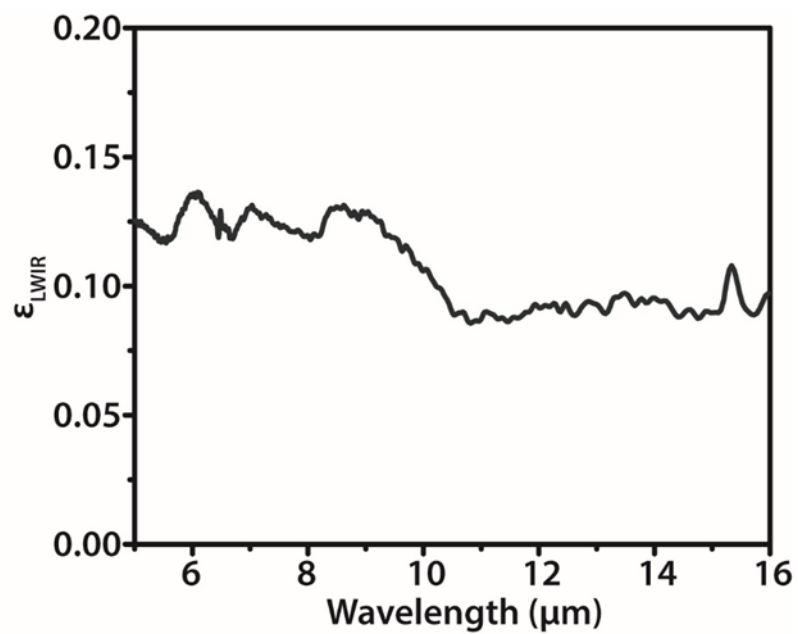


Fig. S3.
 ϵ_{LWIR} spectrum of ITO.

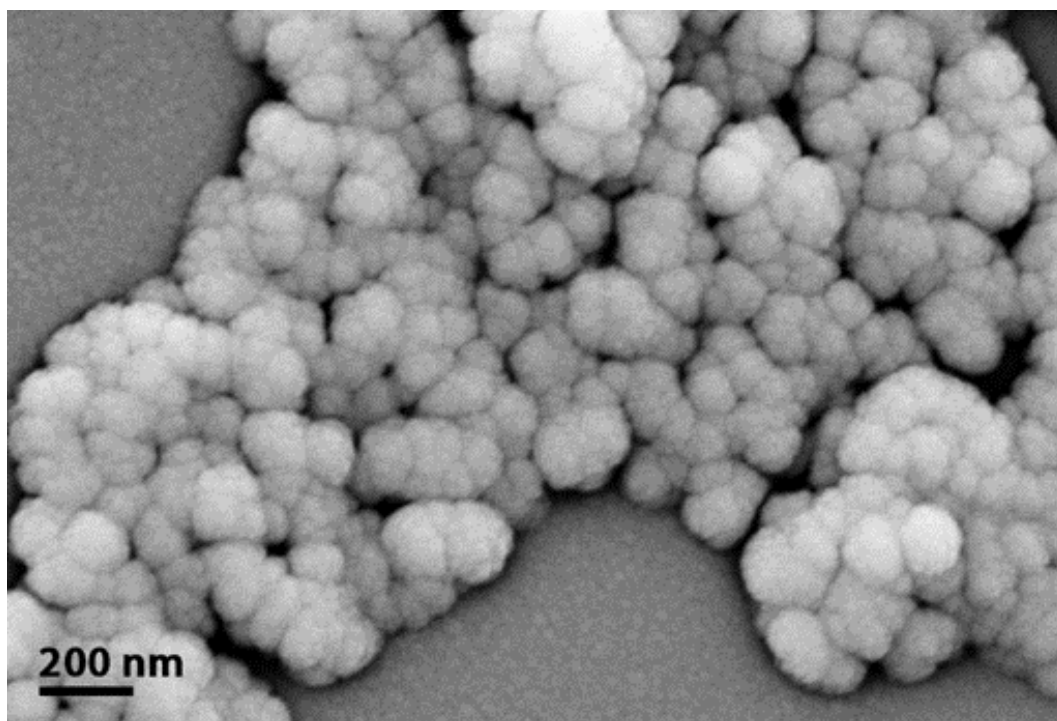


Fig. S4.
SEM image of VO₂ NPs.

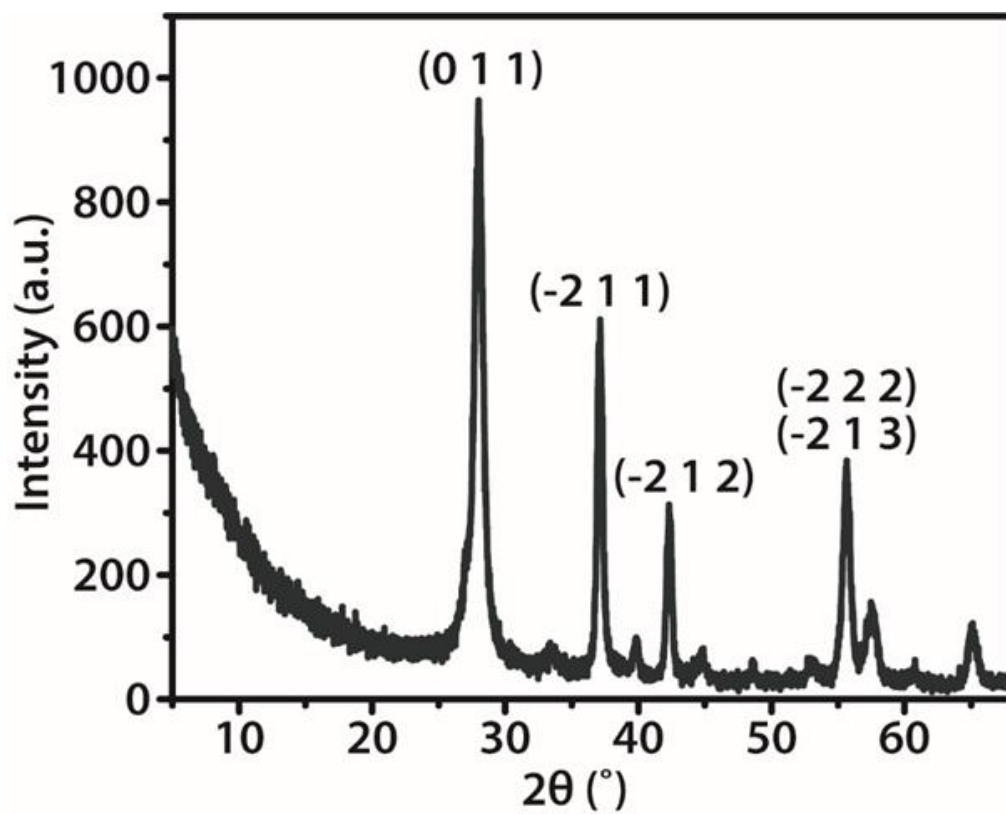


Fig. S5.
XRD pattern of VO₂ NPs.

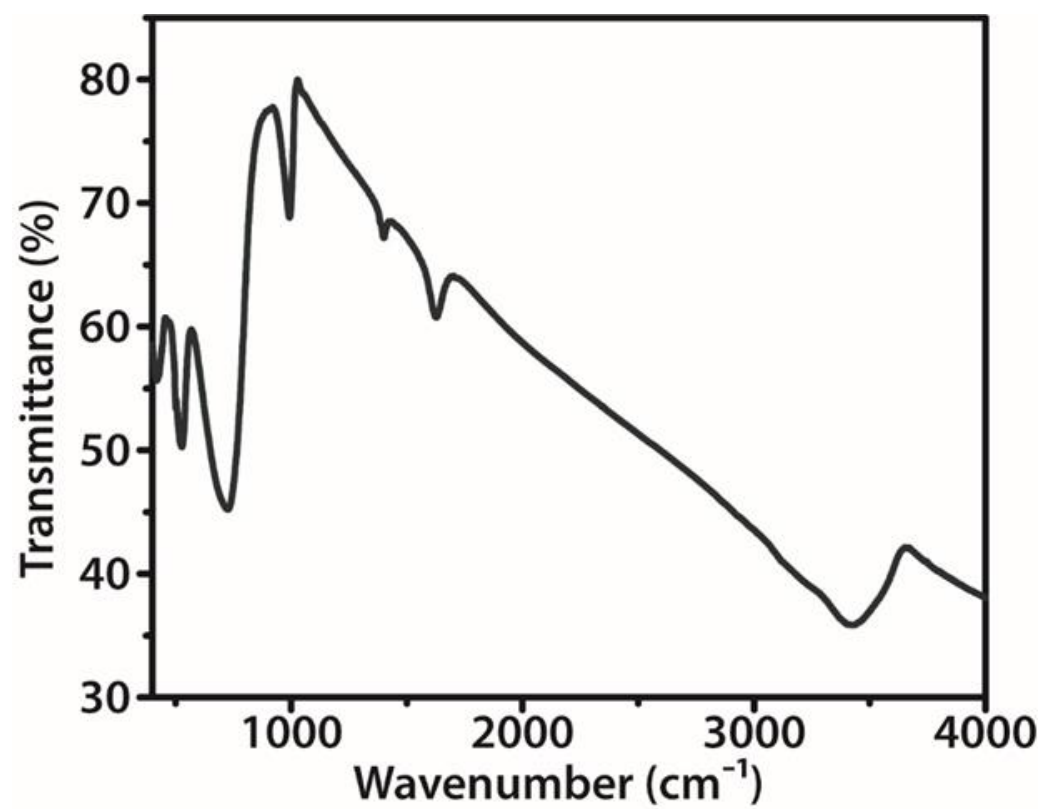


Fig. S6.
FTIR spectrum of VO₂ NPs.

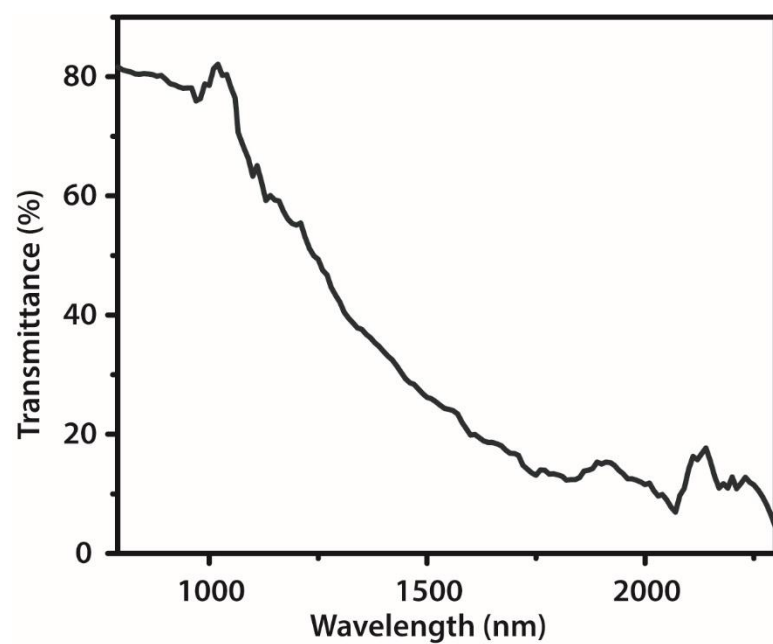


Fig. S7.
NIR transmittance of ITO.

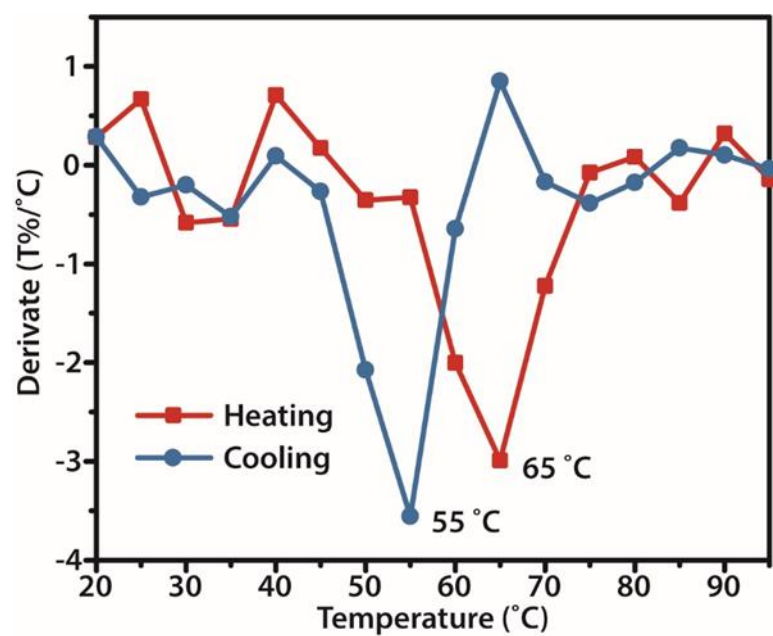


Fig. S8.

Derivate of transmittance for pure VO₂ to show its transition temperature.

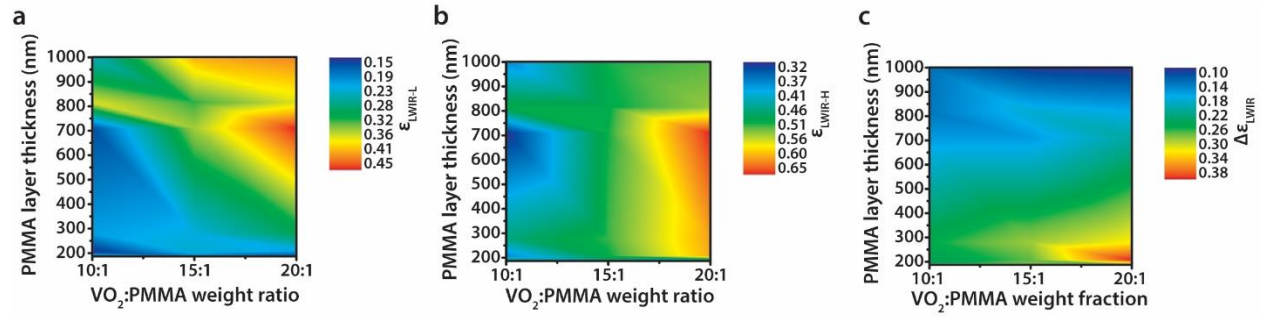


Fig. S9.

Mapping results on the effects of PMMA spacer thickness and VO₂ weight ratio in the VO₂ layer to the (A) $\epsilon_{\text{LWIR-L}}$, (B) $\epsilon_{\text{LWIR-H}}$, (C) $\Delta\epsilon_{\text{LWIR}}$.

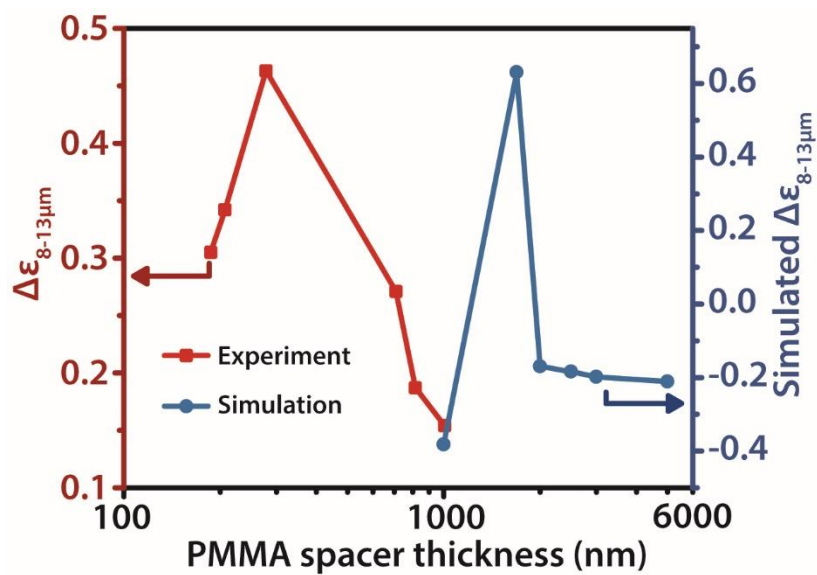


Fig. S10.

Experiment (labelled in red) and simulation (labelled in blue) relationship of $\Delta\epsilon_{8-13\mu m}$ and PMMA spacer thickness with fixed VO_2 weight ratio of 20:1.

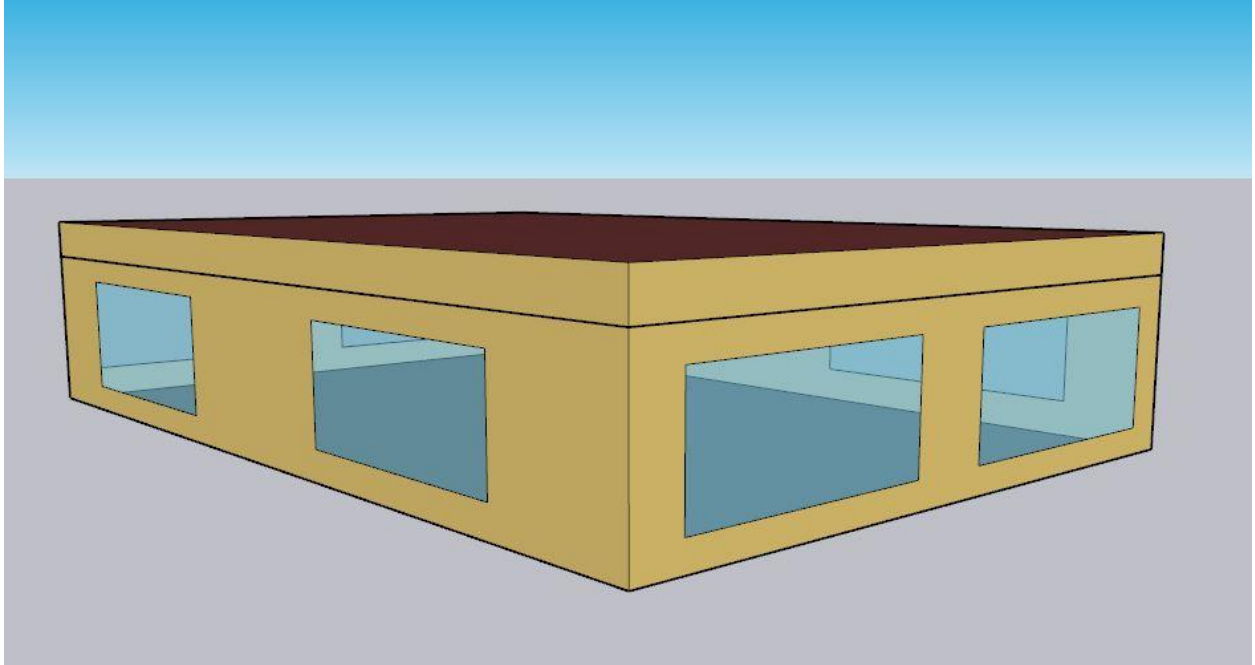


Fig. S11.
Geometrical model of the single-story prototype building for mapping simulation.

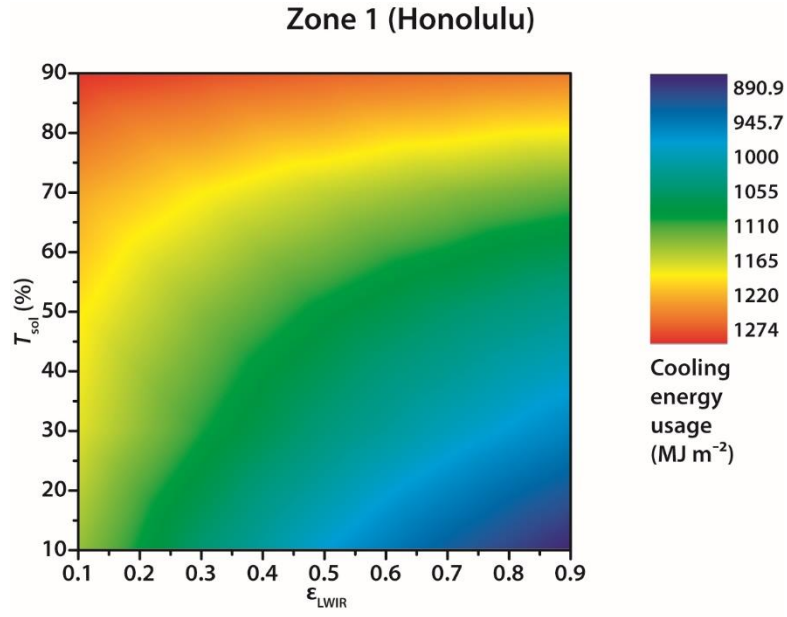


Fig. S12.

Mapping result on the effects of T_{sol} and ϵ_{LWIR} to the cooling energy usage in zone 1. The heating energy consumption in zone 1 is negligible. Colors of the regions indicate the cooling energy usage of samples.

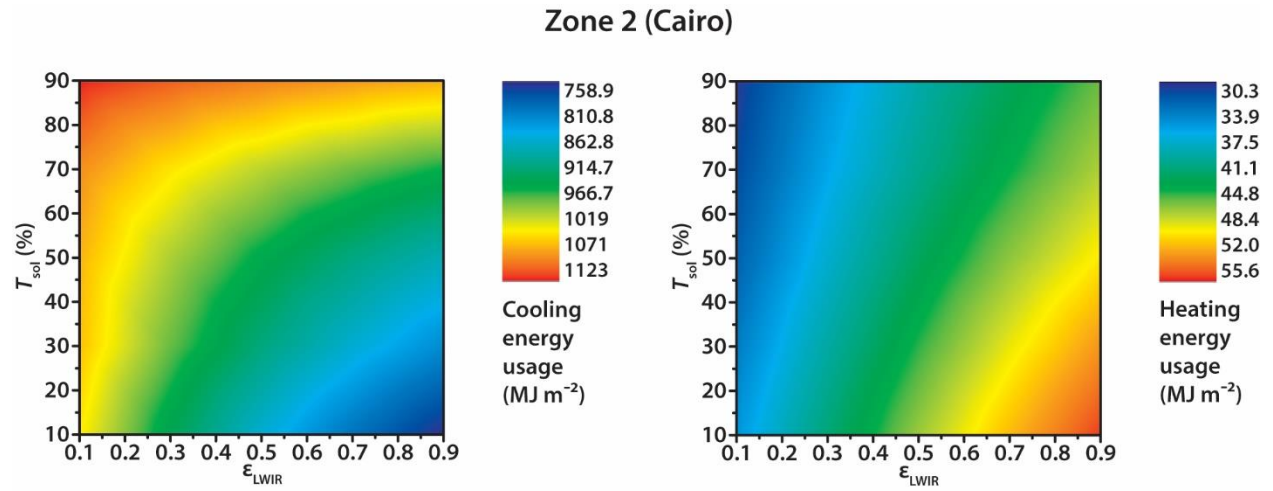


Fig. S13.

Mapping results on the effect of T_{sol} and ϵ_{LWIR} to the cooling (left) and heating (right) energy usage in zone 2. Color of the regions indicates the energy usage of samples, respectively.

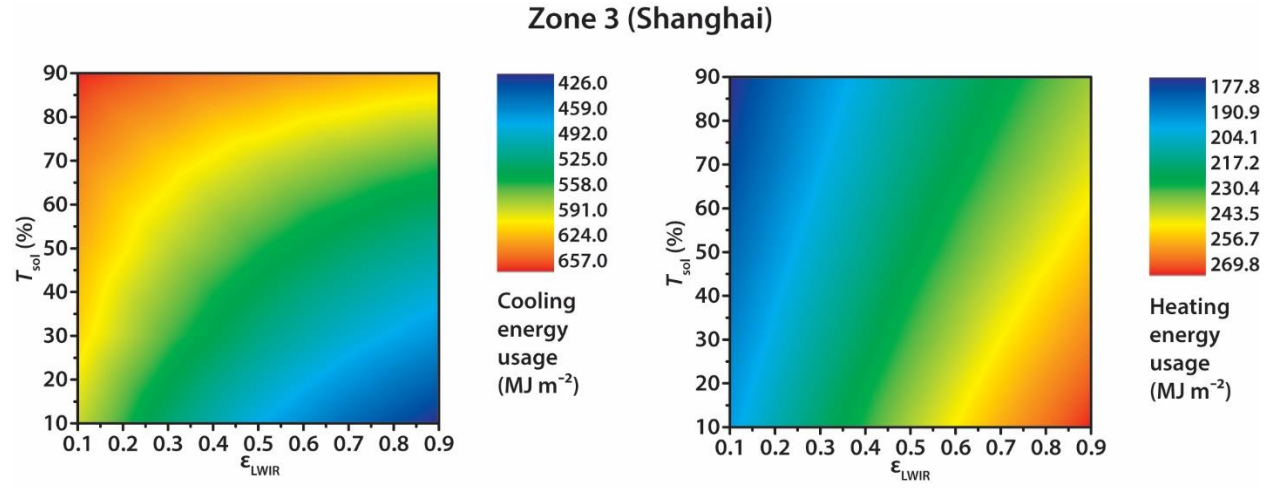


Fig. S14.

Mapping results on the effect of T_{sol} and ϵ_{LWIR} to the cooling (left) and heating (right) energy usage in zone 3. Color of the regions indicates the energy usage of samples, respectively.

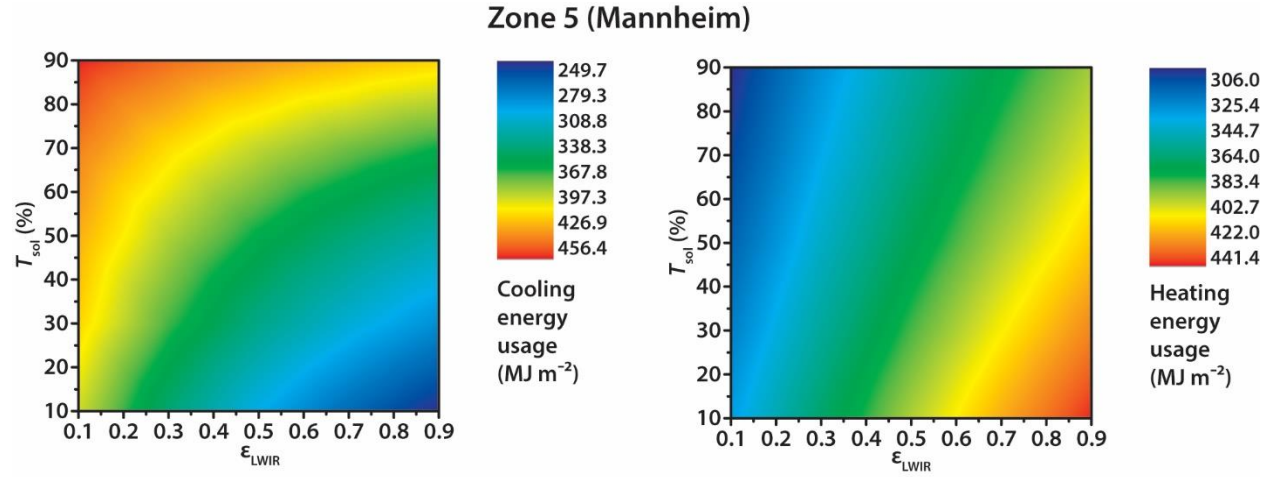


Fig. S15.

Mapping results on the effect of T_{sol} and ϵ_{LWIR} to the cooling (left) and heating (right) usage in zone 5. Color of the regions indicates the energy usage of samples, respectively.

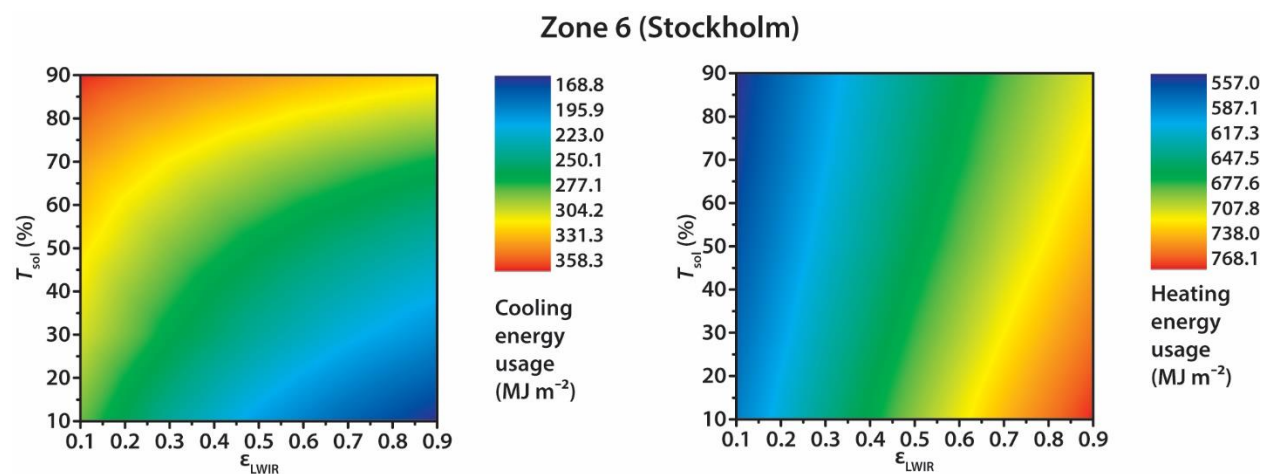


Fig. S16.

Mapping results on the effect of T_{sol} and ϵ_{LWIR} to the cooling (left) and heating (right) energy usage in zone 6. Color of the regions indicates the energy usage of samples, respectively.

Zone 7 (Whitehorse)

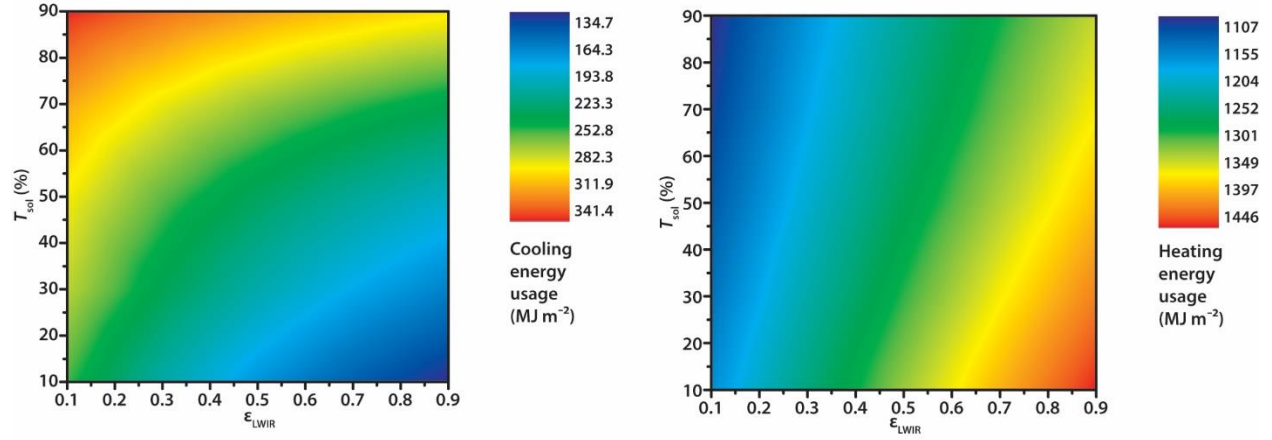


Fig. S17.

Mapping results on the effect of T_{sol} and ϵ_{LWIR} to the cooling (left) and heating (right) energy usage in zone 7. Color of the regions indicates the energy usage of samples, respectively.

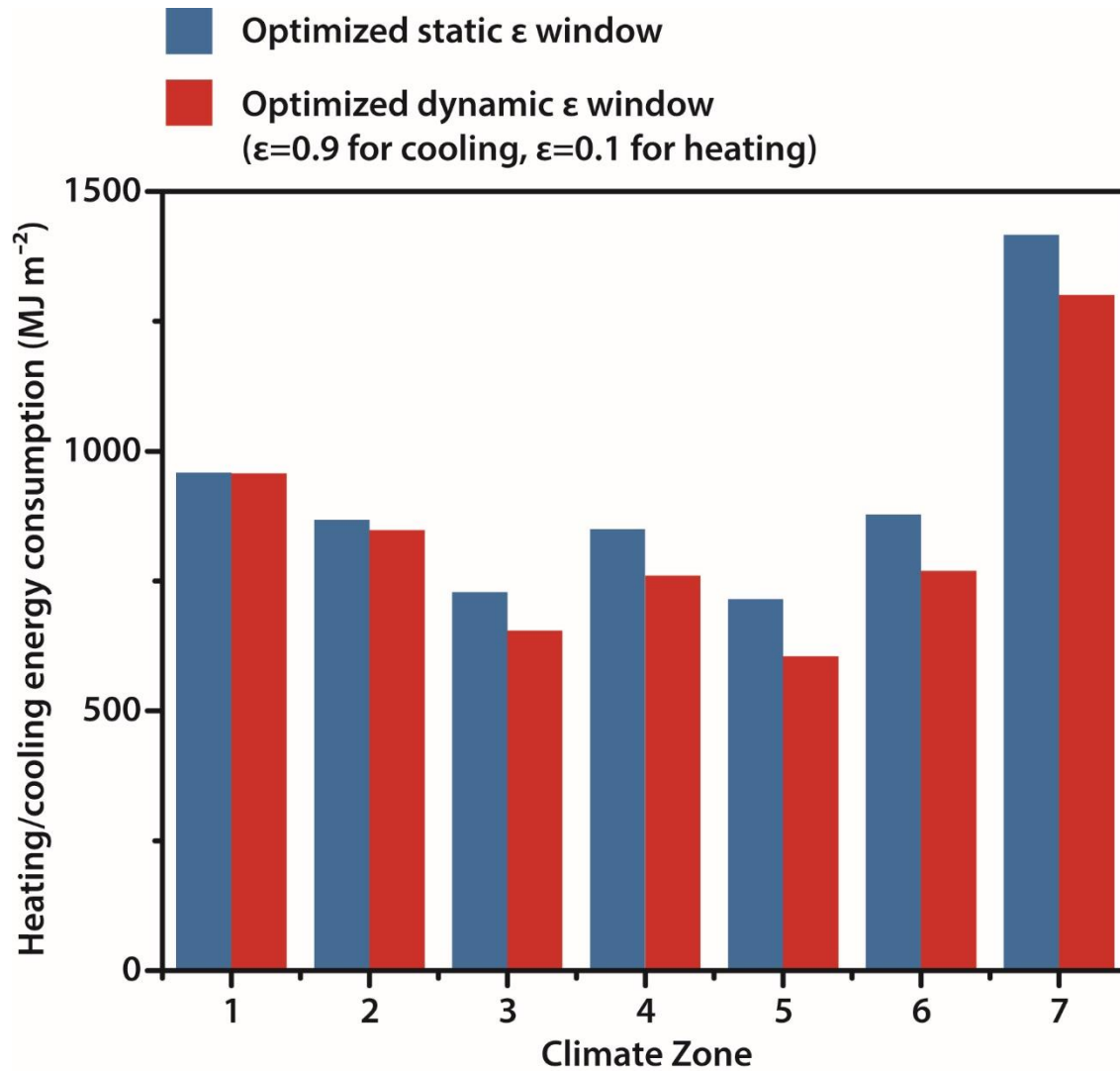


Fig. S18.

Heating/cooling energy consumption of optimized static ϵ window and optimized dynamic ϵ window. The energy consumption of static optimized ϵ window is derived from the point of minimum total energy consumption in 7 climate zones with fixed 30% of T_{sol} . The optimized dynamic ϵ window has a ϵ_{LWIR} of 0.9 for cooling, 0.1 for heating, and a T_{sol} of 30%.

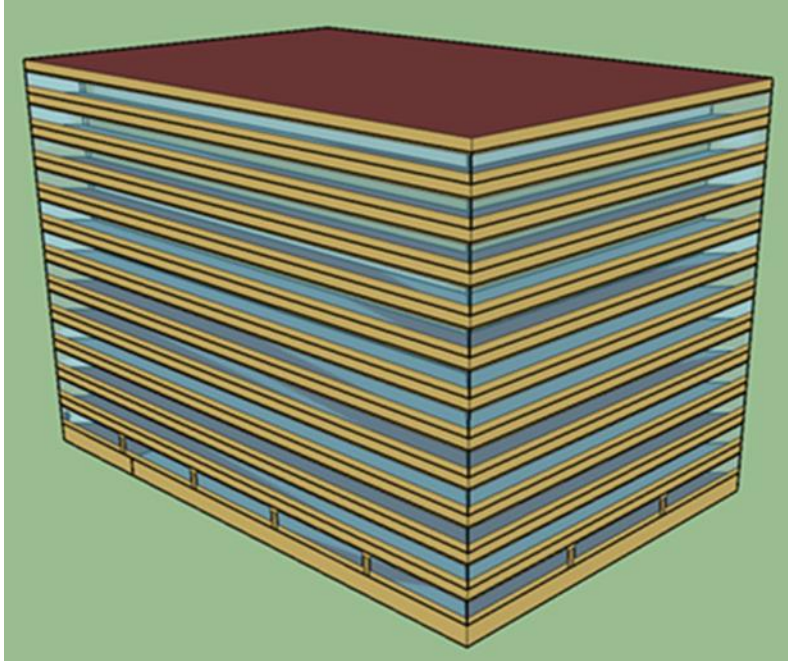


Fig. S19.

Large office building model used in an actual-size building energy simulation. (46)

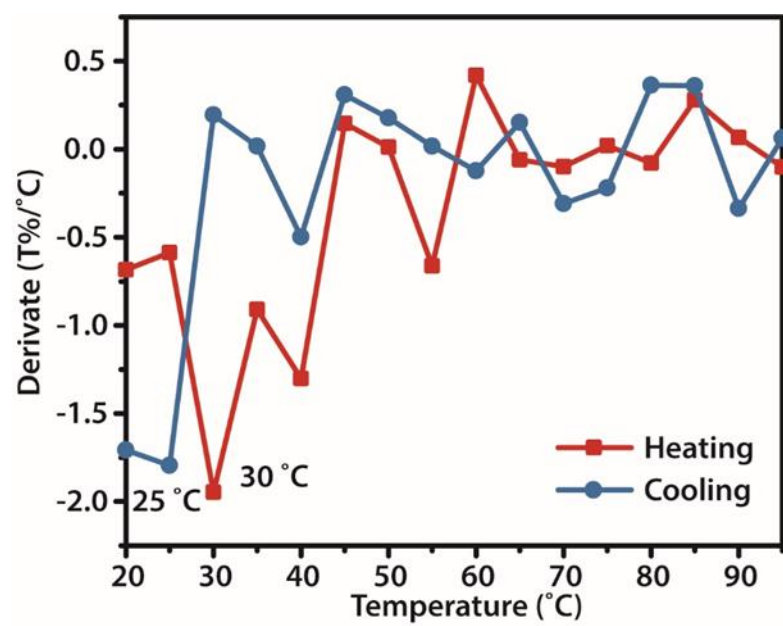


Fig. S20.

Derivate of transmittance for W-doped VO₂ to show its transition temperature.

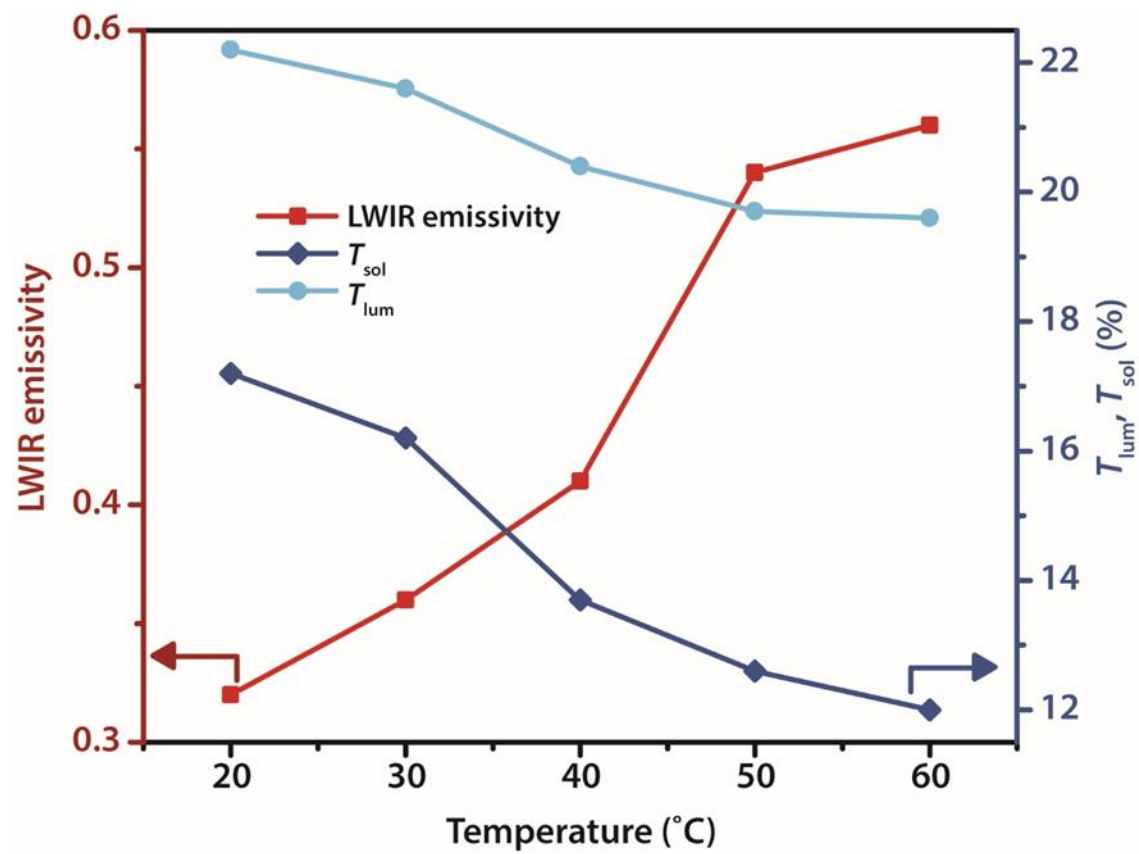


Fig. S21.

T_{lum} , T_{sol} and ϵ_{LWIR} of W-doped VO₂ RCRT window at different temperatures.

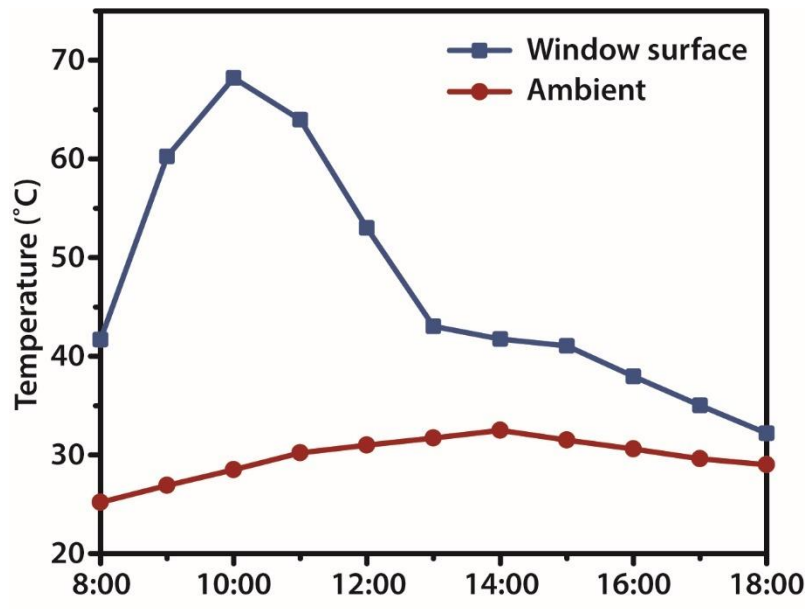


Fig. S22.

Comparison of a simulated eastern window's surface temperature against the ambient temperature from 8:00 to 18:00 for high-rise office building in Singapore.

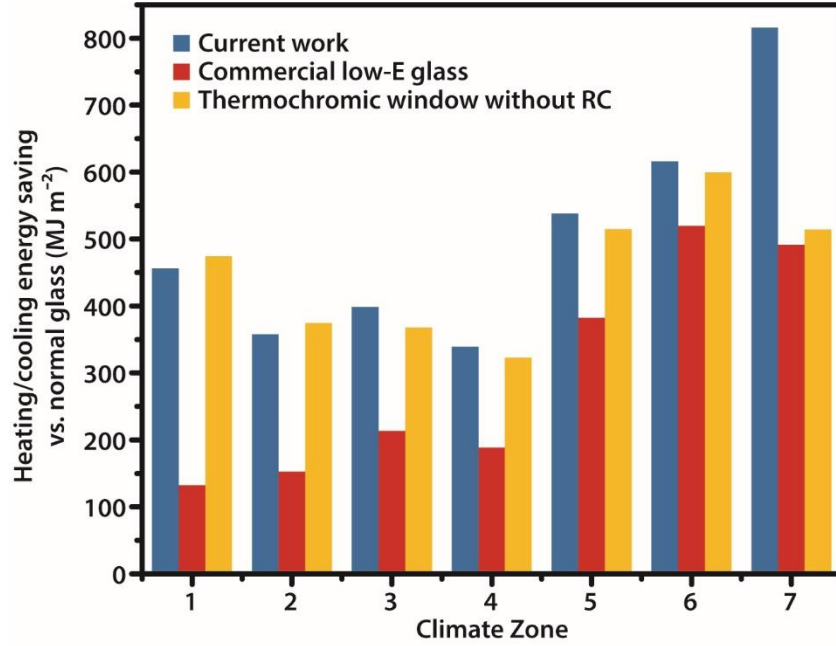


Fig. S23.

Heating/cooling energy savings of commercial low-E glass, W-doped Max $\Delta\epsilon$ sample (namely “current work”) and W-doped VO₂ sample without RC modulation in climate zone 1 to 7 against normal glass and the optical data used in simulation is listed in Table S5. The $\epsilon_{\text{LWIR-Back}}$ of the three glasses are fixed at 0.1 for comparison.

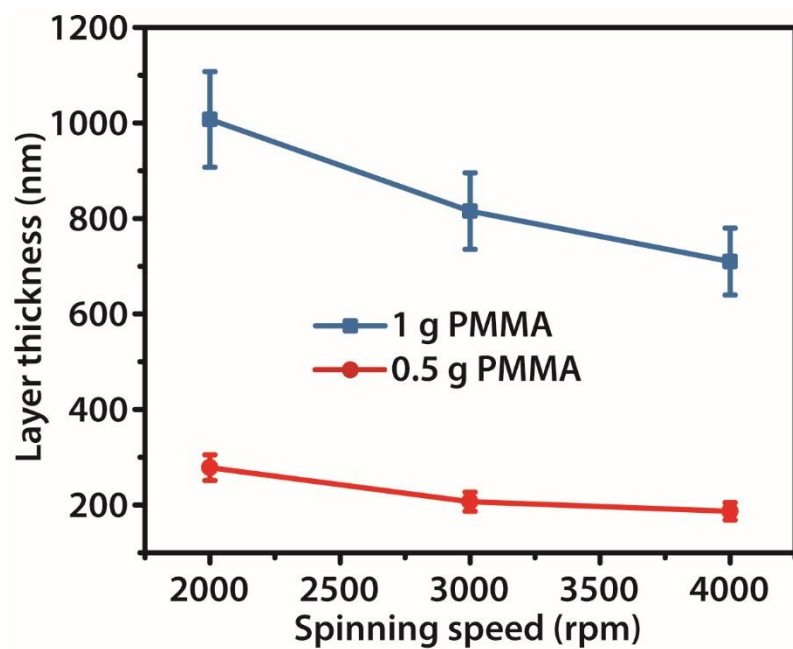


Fig. S24.

Relationship of PMMA film thickness and spinning speed for PMMA-acetone solution with different PMMA content.

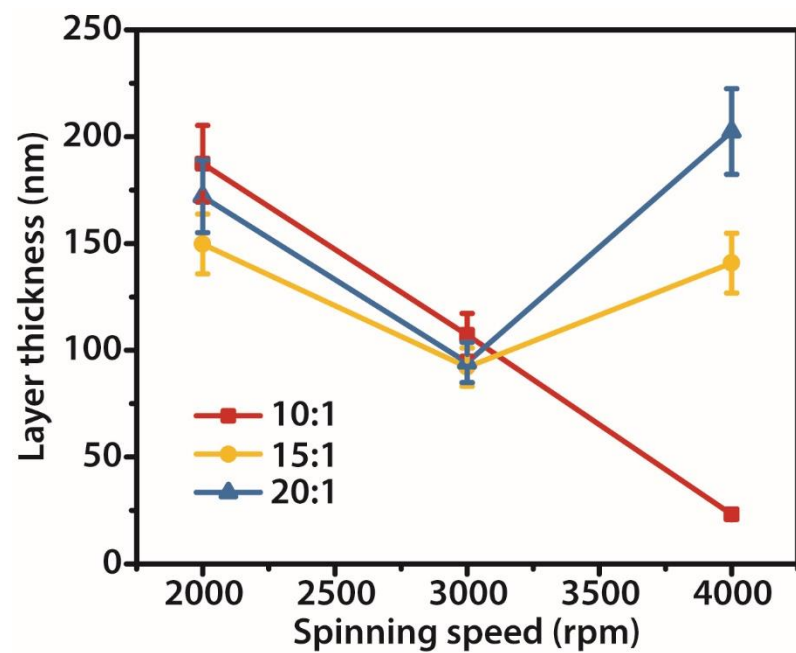


Fig. S25.

Relationships of VO₂ film thickness and spinning speed for different VO₂ weight ratio suspensions.

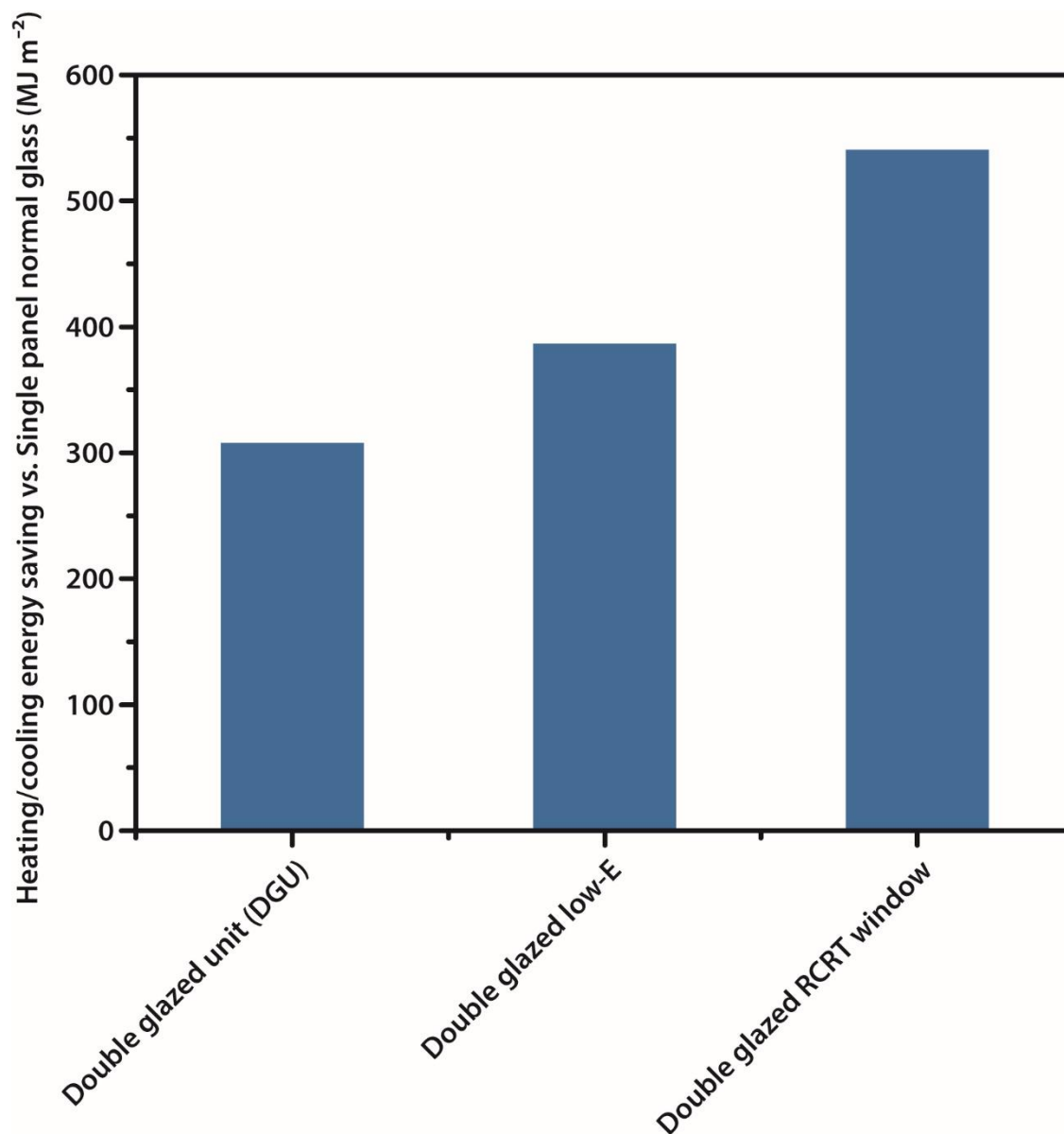


Fig. S26.

Heating and cooling energy saving for double glazed unit, double glazed low-E window, and double glazed RCRT window in Shanghai with the single panel normal glass as baseline. For double glazed RCRT window, RCRT layer is on the surface 1 while the low-E layer is on the surface 2. Optical properties of commercial low-E glass and W-doped Max $\Delta\epsilon$ sample listed in Table S5 were used in this simulation.

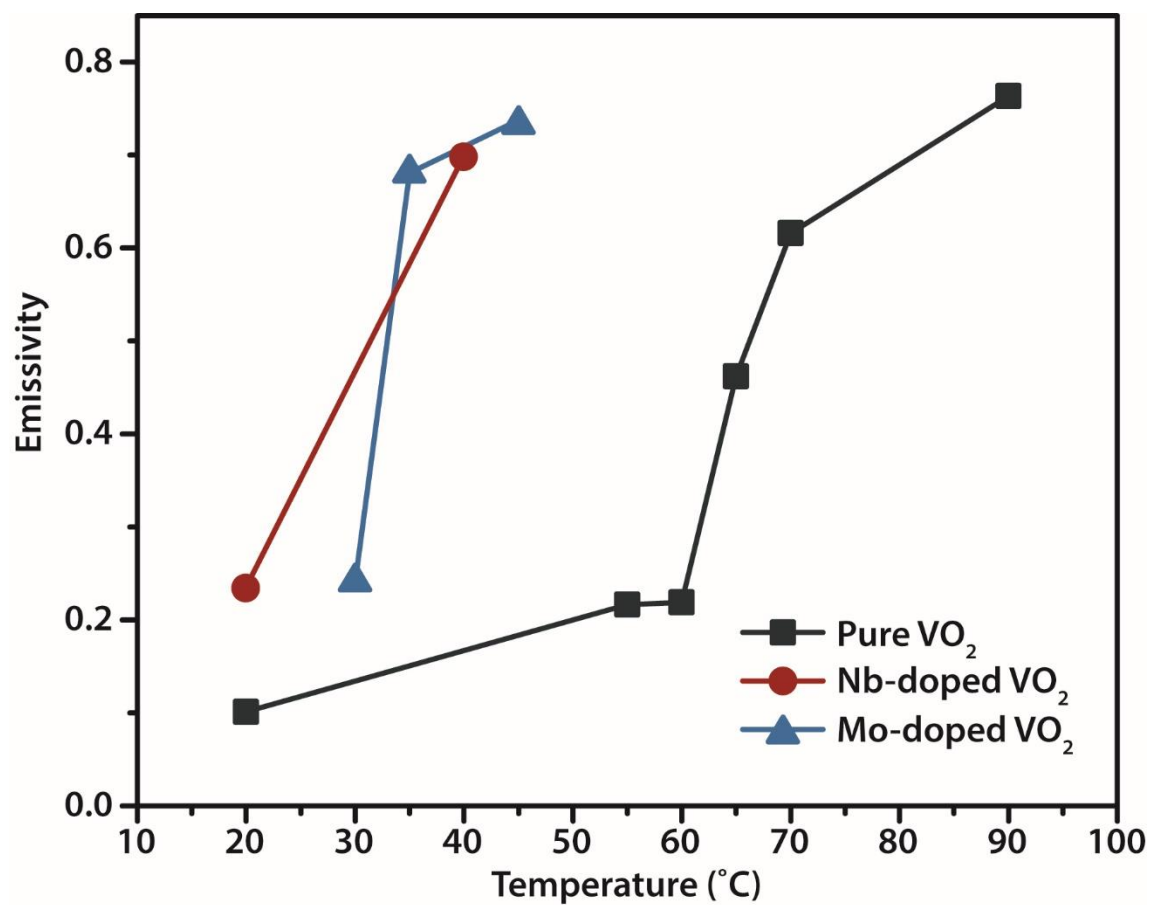


Fig. S27

FDTD simulated emissivity for pure VO₂, Nb-doped VO₂, and Mo-doped VO₂ based RCRT windows at different temperatures.

Table S1.

Summary of recent RC/emissivity regulation works.

Luminous transmission (380-780 nm)	Solar transmission (380-2500 nm)	Atmospheric window emissivity (8-13 μm)	Materials/Structure	Applications	Reference
27.8%	27.4% (20°C) 18.1% (90°C)	0.24 (20°C) 0.70 (90°C)	VO₂-PMMA spacer-ITO	Smart window	This work
N/A* (highly reflective)	N/A (highly reflective)	~0.85	HfO ₂ /SiO ₂ multilayer	Daytime radiative cooler	S. Fan, <i>et al.</i> , <i>Nature</i> , 2014 ⁹
Highly transparent	N/A	~0.95	Silica photonic crystal	Transparent radiative cooler for solar panel	S. Fan, <i>et al.</i> , <i>Proc. Natl. Acad. Sci. U. S. A.</i> , 2015 ¹⁰
N/A (highly reflective)	N/A (highly reflective)	~0.9	Si ₃ N ₄ /Si/Al on Si wafer	Radiative cooler	S. Fan <i>et al.</i> , <i>Nat. Commun.</i> , 2016 ¹¹
Translucent	N/A	>0.93	Polymer-based hybrid metamaterial with randomly distributed SiO ₂ microsphere	Semi-transparent radiative cooling film	X. Yin <i>et al.</i> , <i>Science</i> , 2017 ¹⁵
N/A (black/white opaque emitter)	N/A (black/white opaque emitter)	~0.9	Black/white spray-painted copper emitter	Directional daytime radiative cooler	E. N. Wang <i>et al.</i> , <i>Nat. Commun.</i> , 2018 ¹²
<5%	<5%	0.83	Delignificated hot pressed wood	Radiative cooling structural material	L. Hu <i>et al.</i> , <i>Science</i> , 2019 ²⁰
N/A (highly reflective)	N/A (highly reflective)	~0.95	PDMS coated metal (Al or Ag) film	All-day radiative cooling film	Q. Gan <i>et al.</i> , <i>Nature Sustainability</i> , 2019 ¹⁴
N/A (coloured opaque painting)	N/A (coloured opaque painting)	0.95	Bilayer hierarchically porous polymer film	Coloured radiative cooling painting	Yang, Y. <i>et al.</i> , <i>Sci. Adv.</i> , 2020 ⁶⁰
N/A (white opaque film)	N/A (white opaque film)	0.98	Hierarchically structured PMMA film with a micropore array	Radiative cooling film	L. Wu <i>et al.</i> , <i>Nat. Commun.</i> , 2021 ⁶¹
N/A	N/A	~0.2 (25°C) ~0.8 (70°C)	VO ₂ on sapphire	IR absorber	F. Capasso <i>et al.</i> , <i>Appl. Phys. Lett.</i> , 2012 ³⁰

N/A (highly reflective)	N/A (highly reflective)	~0.1 (Amorphous) ~0.5 (Crystalline) Driven by electricity	Crystalline GST on Au coated glass	Data storage	M. Wuttig <i>et al.</i> , <i>Nat. Mater.</i> , 2008 ⁶²
N/A	N/A	~0.4 (Pristine) ~0.2 (H intercalation)	Perovskite on Si ₃ N ₄	Optical memories	N. Yu <i>et al.</i> , <i>Adv. Mater.</i> , 2016 ⁶³
N/A	N/A	~0.3 (25°C) ~0.8 (100°C)	VO ₂ -SiO ₂ -Au multilayer structure	Thermal radiator	É. Haddad <i>et al.</i> , <i>Appl. Phys. Lett.</i> , 2013 ⁶⁴
N/A	N/A	~0.3 (25°C) ~0.75 (80°C)	VO ₂ -SiO ₂ -Al-Al ₂ O ₃ on Si	Radiative cooler	O. L. Muskens <i>et al.</i> , <i>ACS Photonics</i> 2018 ⁶⁵
N/A	61%	N/A	Simulation work for window energy saving		J. Wang <i>et al.</i> , <i>Appl. Energy</i> , 2015 ⁶⁶
39.6%	~35% (20°C) ~30% (90°C)	~0.2	VO ₂ on FTO	Smart window	Z. L. Wang <i>et al.</i> , <i>Energy Environ. Sci.</i> 2011 ⁶⁷

*N/A: not available

Table S2.

A: Information of the building model applied in mapping simulation.

Items	Specifications
Window fraction (window-to-wall ratio)	30% of above-grade gross walls
Window locations	Even distribution among all four sides
Floor to ceiling height	3.00 m
Glazing sill height	0.70 m
Exterior walls	Stucco + wall insulation + gypsum board
Roof	Roof membrane + roof insulation + roof truss
Window	The window type is described accordingly Ideal-loads-air-system served by district cooling and heating sources; thermostat setpoint 24 °C (75 °F) cooling/ 21 °C (70 °F) heating with 5.6 °C (10 °F) setback
HVAC	

B: Information of the building model applied in actual building energy simulation.

Items	Specifications
Window fraction (window-to-wall ratio)	40% of above-grade gross walls
Window locations	Even distribution among all four sides
Floor to floor height	3.96 m
Floor to ceiling height	2.74 m
Glazing sill height	0.91 m
Exterior walls	Mass (pre-cast concrete panel): heavy-weight concrete + wall insulation + gypsum board
Roof	Built-up roof: roof membrane + roof insulation + metal decking
Window	The window type is described accordingly Water-cooled centrifugal chillers + VAV terminal box with damper and hot-water reheating coil + gas-fired boiler; thermostat setpoint 24 °C (75 °F) cooling/ 21 °C (70 °F) heating with 5.6 °C (10 °F) setback
HVAC	

Table S3.

PMMA spacer thickness and W-doped VO₂ weight ratio to tune the ϵ_{LWIR} (2.5-25 μm) in the RCRT window

$\epsilon_{\text{LWIR-L}}$						
	PMMA spacer thickness (nm)					
W-VO ₂ :PMMA weight ratio	190	210	280	710	820	1000
10:1	0.18	0.16	0.20	0.42	0.45	0.55
15:1	0.16	0.14	0.19	0.48	0.58	0.57
20:1	0.31	0.32	0.36	0.59	0.64	0.65
$\epsilon_{\text{LWIR-H}}$						
	PMMA spacer thickness (nm)					
W-VO ₂ :PMMA weight ratio	190	210	280	710	820	1000
10:1	0.26	0.23	0.25	0.53	0.54	0.59
15:1	0.19	0.19	0.31	0.64	0.69	0.64
20:1	0.52	0.57	0.56	0.77	0.71	0.74
$\Delta\epsilon_{\text{LWIR}}$						
	PMMA spacer thickness (nm)					
W-VO ₂ :PMMA weight ratio	190	210	280	710	820	1000
10:1	0.09	0.07	0.06	0.11	0.09	0.05
15:1	0.03	0.05	0.12	0.15	0.12	0.07
20:1	0.21	0.24	0.20	0.18	0.07	0.09

Table S4.

Summary of the optimized $\varepsilon_{\text{LWIR}}$ and heating/cooling energy consumption of static $\varepsilon_{\text{LWIR}}$ window for different climate zone.

Climate zone	Optimized $\varepsilon_{\text{LWIR}}$	Heating/cooling energy consumption (MJ m^{-2})
Zone 1 (Honolulu)	0.9	958.9
Zone 2 (Cairo)	0.9	867.8
Zone 3 (Shanghai)	0.9	728.7
Zone 4 (Albuquerque)	0.9	849.8
Zone 5 (Mannheim)	0.7	715.2
Zone 6 (Stockholm)	0.1	878.1
Zone 7 (Whitehorse)	0.1	1416.5

Table S5.

Optical properties for samples used in simulation

Optical properties	W-doped Max $\Delta\epsilon$	W-doped VO ₂ w/o RC modulation	Commercial low-E glass	Normal glass
$\epsilon_{\text{LWIR-L}}$	0.32	0.82	0.84	0.84
$\epsilon_{\text{LWIR-H}}$	0.56	0.84	0.84	0.84
$\Delta\epsilon_{\text{LWIR}}$	0.24	0.02	0	0
$\epsilon_{\text{LWIR-Back}}$	0.1	0.1	0.1	0.84
$T_{\text{lum}} (\%)$	22.2	25.5	85.0	88.1
$R_{\text{lum-Front}} (\%)$	9.1	7.9	5.6	8.0
$R_{\text{lum-Back}} (\%)$	11.6	11.3	7.9	8.0
$T_{\text{sol-L}} (\%)$	17.2	23.8	63.0	77.5
$R_{\text{sol-L-Front}} (\%)$	11.1	7.9	19.0	7.1
$R_{\text{sol-L-Back}} (\%)$	16.6	16.6	22.0	7.1
$T_{\text{sol-H}} (\%)$	12.0	16.1	63.0	77.5
$R_{\text{sol-H-Front}} (\%)$	7.7	6.5	19.0	7.1
$R_{\text{sol-H-Back}} (\%)$	16.5	16.7	22.0	7.1

Table S6.

Summary of VO₂-PMMA mixed suspension used in this work.

VO ₂ /PMMA weight ratio	Weight of VO ₂ (g)	Weight of PMMA
10:1	0.5	0.05
15:1	0.75	0.05
20:1	1	0.05

References and Notes

1. L. Zhao, X. Lee, R. B. Smith, K. Oleson, Strong contributions of local background climate to urban heat islands. *Nature* **511**, 216–219 (2014). [doi:10.1038/nature13462](https://doi.org/10.1038/nature13462) [Medline](#)
2. E. Cuce, S. B. Riffat, A state-of-the-art review on innovative glazing technologies. *Renew. Sustain. Energy Rev.* **41**, 695–714 (2015). [doi:10.1016/j.rser.2014.08.084](https://doi.org/10.1016/j.rser.2014.08.084)
3. Y. Gao, S. Wang, L. Kang, Z. Chen, J. Du, X. Liu, H. Luo, M. Kanehira, VO₂-Sb:SnO₂ composite thermochromic smart glass foil. *Energy Environ. Sci.* **5**, 8234–8237 (2012). [doi:10.1039/c2ee21119j](https://doi.org/10.1039/c2ee21119j)
4. E. S. Lee, X. Pang, S. Hoffmann, H. Goudey, A. Thanachareonkit, An empirical study of a full-scale polymer thermochromic window and its implications on material science development objectives. *Sol. Energy Mater. Sol. Cells* **116**, 14–26 (2013). [doi:10.1016/j.solmat.2013.03.043](https://doi.org/10.1016/j.solmat.2013.03.043)
5. Y. Y. Cui, Y. Ke, C. Liu, Z. Chen, N. Wang, L. Zhang, Y. Zhou, S. Wang, Y. Gao, Y. Long, Bridging thermochromic VO₂ with energy-efficient smart windows: A multi-scale perspective from structure to property. *Joule* **2**, 1707–1746 (2018). [doi:10.1016/j.joule.2018.06.018](https://doi.org/10.1016/j.joule.2018.06.018)
6. Y. Ke, J. Chen, G. Lin, S. Wang, Y. Zhou, J. Yin, P. S. Lee, Y. Long, Smart windows: Electro-, thermo-, mechano-, photo-chromics and beyond. *Adv. Energy Mater.* **9**, 1902066 (2019). [doi:10.1002/aenm.201902066](https://doi.org/10.1002/aenm.201902066)
7. S. Wang, K. A. Owusu, L. Mai, Y. Ke, Y. Zhou, P. Hu, S. Magdassi, Y. Long, Vanadium dioxide for energy conservation and energy storage applications: Synthesis and performance improvement. *Appl. Energy* **211**, 200–217 (2018). [doi:10.1016/j.apenergy.2017.11.039](https://doi.org/10.1016/j.apenergy.2017.11.039)
8. C. G. Granqvist, Spectrally selective coatings for energy efficiency and solar applications. *Phys. Scr.* **32**, 401–407 (1985). [doi:10.1088/0031-8949/32/4/026](https://doi.org/10.1088/0031-8949/32/4/026)
9. A. P. Raman, M. A. Anoma, L. Zhu, E. Rephaeli, S. Fan, Passive radiative cooling below ambient air temperature under direct sunlight. *Nature* **515**, 540–544 (2014). [doi:10.1038/nature13883](https://doi.org/10.1038/nature13883) [Medline](#)
10. L. Zhu, A. P. Raman, S. Fan, Radiative cooling of solar absorbers using a visibly transparent photonic crystal thermal blackbody. *Proc. Natl. Acad. Sci. U.S.A.* **112**, 12282–12287 (2015). [doi:10.1073/pnas.1509453112](https://doi.org/10.1073/pnas.1509453112) [Medline](#)
11. Z. Chen, L. Zhu, A. Raman, S. Fan, Radiative cooling to deep sub-freezing temperatures through a 24-h day-night cycle. *Nat. Commun.* **7**, 13729 (2016). [doi:10.1038/ncomms13729](https://doi.org/10.1038/ncomms13729) [Medline](#)
12. B. Bhatia, A. Leroy, Y. Shen, L. Zhao, M. Gianello, D. Li, T. Gu, J. Hu, M. Soljačić, E. N. Wang, Passive directional sub-ambient daytime radiative cooling. *Nat. Commun.* **9**, 5001 (2018). [doi:10.1038/s41467-018-07293-9](https://doi.org/10.1038/s41467-018-07293-9) [Medline](#)
13. J. Mandal, M. Jia, A. Overvig, Y. Fu, E. Che, N. Yu, Y. Yang, Porous polymers with switchable optical transmittance for optical and thermal regulation. *Joule* **3**, 3088–3099 (2019). [doi:10.1016/j.joule.2019.09.016](https://doi.org/10.1016/j.joule.2019.09.016)

14. L. Zhou, H. Song, J. Liang, M. Singer, M. Zhou, E. Stegenburgs, N. Zhang, C. Xu, T. Ng, Z. Yu, B. Ooi, Q. Gan, A polydimethylsiloxane-coated metal structure for all-day radiative cooling. *Nat. Sustain.* **2**, 718–724 (2019). [doi:10.1038/s41893-019-0348-5](https://doi.org/10.1038/s41893-019-0348-5)
15. Y. Zhai, Y. Ma, S. N. David, D. Zhao, R. Lou, G. Tan, R. Yang, X. Yin, Scalable-manufactured randomized glass-polymer hybrid metamaterial for daytime radiative cooling. *Science* **355**, 1062–1066 (2017). [doi:10.1126/science.aai7899](https://doi.org/10.1126/science.aai7899) [Medline](#)
16. D. Zhao, A. Aili, Y. Zhai, J. Lu, D. Kidd, G. Tan, X. Yin, R. Yang, Subambient cooling of water: Toward real-world applications of daytime radiative cooling. *Joule* **3**, 111–123 (2019). [doi:10.1016/j.joule.2018.10.006](https://doi.org/10.1016/j.joule.2018.10.006)
17. E. A. Goldstein, A. P. Raman, S. Fan, Sub-ambient non-evaporative fluid cooling with the sky. *Nat. Energy* **2**, 17143 (2017). [doi:10.1038/nenergy.2017.143](https://doi.org/10.1038/nenergy.2017.143)
18. Z. Chen, L. Zhu, W. Li, S. Fan, Simultaneously and synergistically harvest energy from the sun and outer space. *Joule* **3**, 101–110 (2019). [doi:10.1016/j.joule.2018.10.009](https://doi.org/10.1016/j.joule.2018.10.009)
19. Y. Peng, J. Chen, A. Y. Song, P. B. Catrysse, P.-C. Hsu, L. Cai, B. Liu, Y. Zhu, G. Zhou, D. S. Wu, H. R. Lee, S. Fan, Y. Cui, Nanoporous polyethylene microfibrils for large-scale radiative cooling fabric. *Nat. Sustain.* **1**, 105–112 (2018). [doi:10.1038/s41893-018-0023-2](https://doi.org/10.1038/s41893-018-0023-2)
20. T. Li, Y. Zhai, S. He, W. Gan, Z. Wei, M. Heidarinejad, D. Dalgo, R. Mi, X. Zhao, J. Song, J. Dai, C. Chen, A. Aili, A. Vellore, A. Martini, R. Yang, J. Srebric, X. Yin, L. Hu, A radiative cooling structural material. *Science* **364**, 760–763 (2019). [doi:10.1126/science.aau9101](https://doi.org/10.1126/science.aau9101) [Medline](#)
21. J. Mandal, Y. Fu, A. C. Overvig, M. Jia, K. Sun, N. N. Shi, H. Zhou, X. Xiao, N. Yu, Y. Yang, Hierarchically porous polymer coatings for highly efficient passive daytime radiative cooling. *Science* **362**, 315–319 (2018). [doi:10.1126/science.aat9513](https://doi.org/10.1126/science.aat9513) [Medline](#)
22. H. Ye, X. Meng, B. Xu, Theoretical discussions of perfect window, ideal near infrared solar spectrum regulating window and current thermochromic window. *Energy Build.* **49**, 164–172 (2012). [doi:10.1016/j.enbuild.2012.02.011](https://doi.org/10.1016/j.enbuild.2012.02.011)
23. H. Ye, X. Meng, L. Long, B. Xu, The route to a perfect window. *Renew. Energy* **55**, 448–455 (2013). [doi:10.1016/j.renene.2013.01.003](https://doi.org/10.1016/j.renene.2013.01.003)
24. M. Ono, K. Chen, W. Li, S. Fan, Self-adaptive radiative cooling based on phase change materials. *Opt. Express* **26**, A777–A787 (2018). [doi:10.1364/OE.26.00A777](https://doi.org/10.1364/OE.26.00A777) [Medline](#)
25. C. Xu, M. Colorado Escobar, A. A. Gorodetsky, Stretchable cephalopod-inspired multimodal camouflage systems. *Adv. Mater.* **32**, e1905717 (2020). [doi:10.1002/adma.201905717](https://doi.org/10.1002/adma.201905717) [Medline](#)
26. L. Xiao, H. Ma, J. Liu, W. Zhao, Y. Jia, Q. Zhao, K. Liu, Y. Wu, Y. Wei, S. Fan, K. Jiang, Fast adaptive thermal camouflage based on flexible VO₂/graphene/CNT thin films. *Nano Lett.* **15**, 8365–8370 (2015). [doi:10.1021/acs.nanolett.5b04090](https://doi.org/10.1021/acs.nanolett.5b04090) [Medline](#)
27. M. Li, D. Liu, H. Cheng, L. Peng, M. Zu, Manipulating metals for adaptive thermal camouflage. *Sci. Adv.* **6**, eaba3494 (2020). [doi:10.1126/sciadv.aba3494](https://doi.org/10.1126/sciadv.aba3494) [Medline](#)

28. Y. Ke, C. Zhou, Y. Zhou, S. Wang, S. H. Chan, Y. Long, Emerging thermal-responsive materials and integrated techniques targeting the energy-efficient smart window application. *Adv. Funct. Mater.* **28**, 1800113 (2018). [doi:10.1002/adfm.201800113](https://doi.org/10.1002/adfm.201800113)
29. Y. Zhou, S. Wang, J. Peng, Y. Tan, C. Li, F. Y. C. Boey, Y. Long, Liquid thermo-responsive smart window derived from hydrogel. *Joule* **4**, 2458–2474 (2020). [doi:10.1016/j.joule.2020.09.001](https://doi.org/10.1016/j.joule.2020.09.001)
30. M. A. Kats, D. Sharma, J. Lin, P. Genevet, R. Blanchard, Z. Yang, M. M. Qazilbash, D. N. Basov, S. Ramanathan, F. Capasso, Ultra-thin perfect absorber employing a tunable phase change material. *Appl. Phys. Lett.* **101**, 221101 (2012). [doi:10.1063/1.4767646](https://doi.org/10.1063/1.4767646)
31. S. Taylor, Y. Yang, L. Wang, Vanadium dioxide based Fabry-Perot emitter for dynamic radiative cooling applications. *J. Quant. Spectrosc. Radiat. Transf.* **197**, 76–83 (2017). [doi:10.1016/j.jqsrt.2017.01.014](https://doi.org/10.1016/j.jqsrt.2017.01.014)
32. ANSI/ASHRAE/IES, “Energy standard for building except low-rise residential buildings” (ANSI/ASHRAE/IES, 2019); <https://www.ashrae.org/technical-resources/bookstore/standard-90-1>.
33. X. Yin, R. Yang, G. Tan, S. Fan, Terrestrial radiative cooling: Using the cold universe as a renewable and sustainable energy source. *Science* **370**, 786–791 (2020). [doi:10.1126/science.abb0971](https://doi.org/10.1126/science.abb0971) [Medline](#)
34. G. Wyszecki, W. S. Stiles, *Color Science: Concepts and Methods, Quantitative Data and Formulae*. (Wiley, New York, ed. 2, 2000).
35. American Society for Testing and Materials, “ASTM G173 Standard tables of reference solar spectral irradiances: direct normal and hemispherical on a 37° tilted surface” (ASTM, 2012).
36. T. Inoue, M. De Zoysa, T. Asano, S. Noda, Realization of dynamic thermal emission control. *Nat. Mater.* **13**, 928–931 (2014). [doi:10.1038/nmat4043](https://doi.org/10.1038/nmat4043) [Medline](#)
37. S.-H. Wu, M. Chen, M. T. Barako, V. Jankovic, P. W. C. Hon, L. A. Sweatlock, M. L. Povinelli, Thermal homeostasis using microstructured phase-change materials. *Optica* **4**, 1390–1396 (2017). [doi:10.1364/OPTICA.4.001390](https://doi.org/10.1364/OPTICA.4.001390)
38. J. B. Kana Kana, G. Vignaud, A. Gibaud, M. Maaza, Thermally driven sign switch of static dielectric constant of VO₂ thin film. *Opt. Mater.* **54**, 165–169 (2016). [doi:10.1016/j.optmat.2016.02.032](https://doi.org/10.1016/j.optmat.2016.02.032)
39. S. Tsuda, S. Yamaguchi, Y. Kanamori, H. Yugami, Spectral and angular shaping of infrared radiation in a polymer resonator with molecular vibrational modes. *Opt. Express* **26**, 6899–6915 (2018). [doi:10.1364/OE.26.006899](https://doi.org/10.1364/OE.26.006899) [Medline](#)
40. T. A. F. König, P. A. Ledin, J. Kerszulis, M. A. Mahmoud, M. A. El-Sayed, J. R. Reynolds, V. V. Tsukruk, Electrically tunable plasmonic behavior of nanocube-polymer nanomaterials induced by a redox-active electrochromic polymer. *ACS Nano* **8**, 6182–6192 (2014). [doi:10.1021/nn501601e](https://doi.org/10.1021/nn501601e) [Medline](#)
41. M. Rubin, Optical properties of soda lime silica glasses. *Sol. Energy Mater.* **12**, 275–288 (1985). [doi:10.1016/0165-1633\(85\)90052-8](https://doi.org/10.1016/0165-1633(85)90052-8)

42. J. W. Cleary, E. M. Smith, K. D. Leedy, G. Grzybowski, J. Guo, Optical and electrical properties of ultra-thin indium tin oxide nanofilms on silicon for infrared photonics. *Opt. Mater. Express* **8**, 1231–1245 (2018). [doi:10.1364/OME.8.001231](https://doi.org/10.1364/OME.8.001231)
43. ANSI/ASHRAE/IES, “Energy standard for building except low-rise residential buildings” (ANSI/ASHRAE/IES, 2016); https://www.ashrae.org/file%20library/technical%20resources/standards%20and%20guidelines/standards%20addenda/90.1-2016/90_1_2016_mai_au_az_bg_dn_20210324.pdf.
44. H.-W. Dong, S.-J. Lee, D.-S. Yoon, J.-Y. Park, J.-W. Jeong, Impact of district heat source on primary energy savings of a desiccant-enhanced evaporative cooling system. *Energy* **123**, 432–444 (2017). [doi:10.1016/j.energy.2017.02.005](https://doi.org/10.1016/j.energy.2017.02.005)
45. R. Goel, X. Athalye, H. Wang, M. Zhang, “Enhancements to ASHRAE standard 90.1 prototype building models,” (US Department of Energy Office of Scientific and Technical Information, 2014); <https://www.osti.gov/biblio/1129366/>.
46. M. Deru, K. Field, D. Studer, K. Benne, B. Griffith, P. Torcellini, B. Liu, M. Halverson, D. Winiarski, M. Rosenberg, M. Yazdanian, J. Huang, D. Crawley, “US Department of Energy commercial reference building models of the national building stock” (US Department of Energy, 2011); <https://www.nrel.gov/docs/fy11osti/46861.pdf>.
47. C. Curcija, S. Vidanovic, R. Hart, J. Jonsson, R. Powles, R. Mitchell, “WINDOW Technical Documentation” (Lawrence Berkeley National Laboratory, 2018).
48. US Environmental Protection Agency, “Portfolio manager technical reference: Source energy” (EPA, 2020); <https://www.energystar.gov/buildings/tools-and-resources/portfolio-manager-technical-reference-source-energy>.
49. D. D’Agostino, L. Mazzarella, What is a Nearly zero energy building? Overview, implementation and comparison of definitions. *J. Build. Eng.* **21**, 200–212 (2019). [doi:10.1016/j.jobbe.2018.10.019](https://doi.org/10.1016/j.jobbe.2018.10.019)
50. L. N. Troup, D. J. Fannon, M. J. Eckelman, Spatio-temporal changes among site-to-source conversion factors for building energy modeling. *Energy Build.* **213**, 109832 (2020). [doi:10.1016/j.enbuild.2020.109832](https://doi.org/10.1016/j.enbuild.2020.109832)
51. E. Molenbroek, E. Stricker, T. Boermans, “Primary energy factors for electricity in buildings: Toward a flexible electricity supply” (Ecofys, 2011); http://download.dalicloud.com/fis/download/66a8abe211271fa0ec3e2b07/ad5fccc2-4811-434a-8c4f-6a2daa41ad2a/Primary_energy_factors_report_ecofys_29.09.2011.pdf.
52. P. Beagon, F. Boland, M. Saffari, Closing the gap between simulation and measured energy use in home archetypes. *Energy Build.* **224**, 110244 (2020). [doi:10.1016/j.enbuild.2020.110244](https://doi.org/10.1016/j.enbuild.2020.110244)
53. J. Oltmanns, M. Freystein, F. Dammel, P. Stephan, Improving the operation of a district heating and a district cooling network. *Energy Procedia* **149**, 539–548 (2018). [doi:10.1016/j.egypro.2018.08.218](https://doi.org/10.1016/j.egypro.2018.08.218)

54. M. I. Iqbal, R. Himmler, S. H. Gheewala, Potential life cycle energy savings through a transition from typical to energy plus households: A case study from Thailand. *Energy Build.* **134**, 295–305 (2017). [doi:10.1016/j.enbuild.2016.11.002](https://doi.org/10.1016/j.enbuild.2016.11.002)
55. M. Jarre, M. Noussan, M. Simonetti, Primary energy consumption of heat pumps in high renewable share electricity mixes. *Energy Convers. Manage.* **171**, 1339–1351 (2018). [doi:10.1016/j.enconman.2018.06.067](https://doi.org/10.1016/j.enconman.2018.06.067)
56. J. Kurnitski, A. Saari, T. Kalamees, M. Vuolle, J. Niemelä, T. Tark, Cost optimal and nearly zero (nZEB) energy performance calculations for residential buildings with REHVA definition for nZEB national implementation. *Energy Build.* **43**, 3279–3288 (2011). [doi:10.1016/j.enbuild.2011.08.033](https://doi.org/10.1016/j.enbuild.2011.08.033)
57. M. C. Cakir, H. Kocer, Y. Durna, D. U. Yildirim, A. Ghobadi, H. Hajian, K. Aydin, H. Kurt, N. Saglam, E. Ozbay, Unveiling the optical parameters of vanadium dioxide in the phase transition region: A hybrid modeling approach. *RSC Advances* **10**, 29945–29955 (2020). [doi:10.1039/D0RA05890D](https://doi.org/10.1039/D0RA05890D)
58. H. M. Pinto, J. Correia, R. Binions, C. Piccirillo, I. P. Parkin, V. Teixeira, Determination of the optical constants of VO₂ and Nb-doped VO₂ Thin Films. *Mater. Sci. Forum* **587-588**, 640–644 (2008). [doi:10.4028/www.scientific.net/MSF.587-588.640](https://doi.org/10.4028/www.scientific.net/MSF.587-588.640)
59. S. Amador-Alvarado, J. M. Flores-Camacho, A. Solís-Zamudio, R. Castro-García, J. S. Pérez-Huerta, E. Antúnez-Cerón, J. Ortega-Gallegos, J. Madrigal-Melchor, V. Agarwal, D. Ariza-Flores, Temperature-dependent infrared ellipsometry of Mo-doped VO₂ thin films across the insulator to metal transition. *Sci. Rep.* **10**, 8555 (2020). [doi:10.1038/s41598-020-65279-4](https://doi.org/10.1038/s41598-020-65279-4) [Medline](#)
60. Y. Chen, J. Mandal, W. Li, A. Smith-Washington, C.-C. Tsai, W. Huang, S. Shrestha, N. Yu, R. P. S. Han, A. Cao, Y. Yang, Colored and paintable bilayer coatings with high solar-infrared reflectance for efficient cooling. *Sci. Adv.* **6**, eaaz5413 (2020). [doi:10.1126/sciadv.aaz5413](https://doi.org/10.1126/sciadv.aaz5413) [Medline](#)
61. T. Wang, Y. Wu, L. Shi, X. Hu, M. Chen, L. Wu, A structural polymer for highly efficient all-day passive radiative cooling. *Nat. Commun.* **12**, 365 (2021). [doi:10.1038/s41467-020-20646-7](https://doi.org/10.1038/s41467-020-20646-7) [Medline](#)
62. K. Shportko, S. Kremers, M. Woda, D. Lencer, J. Robertson, M. Wuttig, Resonant bonding in crystalline phase-change materials. *Nat. Mater.* **7**, 653–658 (2008). [doi:10.1038/nmat2226](https://doi.org/10.1038/nmat2226) [Medline](#)
63. Z. Li, Y. Zhou, H. Qi, Q. Pan, Z. Zhang, N. N. Shi, M. Lu, A. Stein, C. Y. Li, S. Ramanathan, N. Yu, Correlated perovskites as a new platform for super-broadband-tunable photonics. *Adv. Mater.* **28**, 9117–9125 (2016). [doi:10.1002/adma.201601204](https://doi.org/10.1002/adma.201601204) [Medline](#)
64. A. Hendaoui, N. Émond, M. Chaker, É. Haddad, Highly tunable-emittance radiator based on semiconductor-metal transition of VO₂ thin films. *Appl. Phys. Lett.* **102**, 061107 (2013). [doi:10.1063/1.4792277](https://doi.org/10.1063/1.4792277)
65. K. Sun, C. A. Riedel, A. Urbani, M. Simeoni, S. Mengali, M. Zalkovskij, B. Bilenberg, C. H. de Groot, O. L. Muskens, VO₂ thermochromic metamaterial-based smart optical solar reflector. *ACS Photonics* **5**, 2280–2286 (2018). [doi:10.1021/acsphotonics.8b00119](https://doi.org/10.1021/acsphotonics.8b00119)

66. J. Yang, Z. Xu, H. Ye, X. Xu, X. Wu, J. Wang, Performance analyses of building energy on phase transition processes of VO₂ windows with an improved model. *Appl. Energy* **159**, 502–508 (2015). [doi:10.1016/j.apenergy.2015.08.130](https://doi.org/10.1016/j.apenergy.2015.08.130)
67. Z. Zhang, Y. Gao, H. Luo, L. Kang, Z. Chen, J. Du, M. Kanehira, Y. Zhang, Z. L. Wang, Solution-based fabrication of vanadium dioxide on F:SnO₂ substrates with largely enhanced thermochromism and low-emissivity for energy-saving applications. *Energy Environ. Sci.* **4**, 4290–4297 (2011). [doi:10.1039/c1ee02092g](https://doi.org/10.1039/c1ee02092g)